Modelling crack growth rates in a pressurized water reactor environment using the CGR-1 software

Benedikt Martens

Academic year 2007-2008

Promotor: ***Prof. dr. Eric van Walle, KU Leuven***

Thesis submitted in partial fulfilment of the requirements for the degree of Master of Science in Nuclear Engineering

Modelling crack growth rates in a pressurized water reactor environment using the CGR-1 software

Benedikt Martens

Academic year 2007-2008

Promotor: ***Prof. dr. Eric van Walle, KU Leuven***

Thesis submitted in partial fulfilment of the requirements for the degree of Master of Science in Nuclear Engineering

Master of Science in Nuclear Engineering

Thesis Summary Page

Name of the student:

Benedikt Martens

Title:

Modelling crack growth rates in a pressurized water reactor environment using the CGR-1 software

Abstract:

The lifetime of some pressurized water reactor components could be limited because of stress corrosion cracking. Hence, research into the modelling of the crack growth rate in stainless steel is very important. The crack growth rate modelling software, CGR-1, was developed as part of the EU's FP6 project PERFECT by VUB in collaboration with SCK•CEN.
In this thesis a literature study on crack propagation models will be followed by a brief description of the CGR-1 software. A calibration of the software will be carried against a reference dataset for different percentages cold work. The change in crack growth rate will be studied by altering several input parameters like the environmental conditions, the material properties and the crack geometry. The last part of the thesis consists of an evaluation of the results that will be obtained from the CGR-1 software.

Promotor: Prof. dr. Eric van Walle

Mentor: Ir. Marc Vankeerberghen

Assessors: Prof. dr. ir. Patricia Verleysen
Prof. dr. ir. Johan Deconinck

Academic Year 2007-2008

Belgian Nuclear Higher Education Network, c/o SCK•CEN, Boeretang 200, BE-2400 Mol, Belgium

Preface

The subject of this thesis was proposed on the BNEN website in the beginning of November, 2007. After some discussion with my mentor, the outline for the thesis became more obvious and the real work could finally begin in January 2008.
This thesis is the result of an extensive study with respect to the important aspects of stress corrosion cracking and, more specific, the assessment of crack growth rates.

I would like to thank Rachid Chaouadi and Marc Scibetta for their remarks and suggestions for the text of this thesis.
I also would like to acknowledge my promoter, Eric van Walle, for his time, support and useful comments.
Finally, I would like to thank my mentor, Marc Vankeerberghen, for the provision of literature data, additional information, recommendations and his patience.
Without all these people, this thesis would not have become what it is.

1 Introduction 1
2 Stress corrosion cracking 2
2.1 Introduction 2
2.2 The Stress corrosion cracking process 3
2.2.1 Introduction 3
2.2.2 Crack initiation 3
2.2.3 Crack propagation 3
2.2.4 Final failure 3
2.3 Environmental factors 4
2.3.1 Introduction 4
2.3.2 Thermodynamics of SCC 4
2.3.3 Kinetics of SCC 4
2.3.4 Hydrogen embrittlement 4
2.4 Material-related factors 5
2.4.1 Introduction 5
2.4.2 Intergranular stress corrosion cracking 5
2.4.3 Transgranular stress corrosion cracking 5
2.5 Mechanical factors 5
2.6 Crack propagation mechanisms 6
2.6.1 Introduction 6
2.6.2 Dissolution models 6
2.6.3 Mechanical fracture models 6
2.7 Conclusion 7
3 The film rupture/repassivation model 8
3.1 Introduction 8
3.2 The slip dissolution model 8
3.2.1 Introduction 8
3.2.2 Mathematical derivation 8
3.3 The crack tip strain rate 11
3.3.1 Introduction 11
3.3.2 Plane strain crack tip strain rate 11
3.3.3 Plane stress crack tip strain rate 12
4 CGR-1 14
4.1 Introduction 14
4.2 Slip dissolution and crack tip strain rate 14
4.2.1 Introduction 14
4.2.2 The analytical model 14
4.3 The environment 16
4.3.1 Introduction 16
4.3.2 Crack geometry 16
4.3.3 Fluid flow 17
4.3.4 Chemistry/Electrochemistry 18
4.3.5 Homogeneous reactions 18
4.3.6 Diffusion coefficients 20
4.3.7 Electrochemical reactions 22
4.4 Calculation procedure 22
5 Calibration of CGR-1 at reference temperature 320°C 24
5.1 Introduction 24
5.2 Calibration procedure 24

5.3 The input matrix calibration set 25
5.4 Calibration against reference dataset 27
5.5 Discussion and conclusions 32
6 Temperature calibration of CGR-1 33
6.1 Introduction 33
6.2 The input matrix calibration set 33
6.3 The calibration 35
6.4 Discussion and conclusions 38
7 Effect of stress intensity 40
7.1 Introduction 40
7.2 Trend calculation 40
7.2.1 Relation CPR-K 40
7.3 Plane stress versus plane strain 41
7.4 Plane stress or plane strain 43
7.5 CGR-1 with plane strain 43
7.6 Discussion and conclusions 45
8 Trend calculations with CGR-1 48
8.1 Introduction 48
8.2 Repassivation parameter m 48
8.3 Crack length L 49
8.4 Reynolds number Re 49
8.5 Hydrogen concentration H2 50
8.6 Boron and lithium concentration B, Li 50
8.7 Conclusions 52
9 Recommendations and conclusions 53
9.1 Introduction 53
9.2 Recommendations 53
9.3 Conclusions 55
10 References 56
11 List of figures 57

Nomenclature

$\dot{a}$, CPR, CGR	crack propagation rate, crack growth rate
A	parameter from calibration procedure
B	boric acid concentration
B	thickness of CT specimen
C, C_i	concentration of species
D, D_i	diffusion coefficient of species
E	electrode potential
E	Young's elasticity modulus
E_a	activation energy
E_{tip}	electrode potential at the crack tip
F	Faraday's constant
H_2	dissolved hydrogen concentration
i	current density
i_{avg}, I_{tip}	average current density
i_0	sensitization factor
$\hat{i}_0$	maximum current density at moment of film rupture
$\hat{i}^0_0$	pre-exponential from calibration procedure
k	reaction rates
K	stress intensity factor
$\dot{K}$	loading rate
L	crack length
L	width of the central channel
Li	lithium hydroxide concentration
m	repassivation parameter
M	atomic weight
n	number of electrons involved in reaction
n	strain hardening exponent
N_i	flux of "i" species in the environment
O_2	dissolved oxygen concentration
p	hydrostatic pressure
Q_d	charge density
Q_i	reaction equilibrium constants
r	distance ahead of advancing crack tip
R	universal gas constant
Re	Reynolds number
$R_{k,I}$	production term of species in reaction k
Rp	plastic zone size
t	time
t_0	time at which material starts to repassivate
t_f	time to film rupture
T	temperature
U, ϕ_M^L	electrode potential of the solution
v	fluid velocity
V_m	molar volume
z, z_i	charge
α_i, α	anodic transfer coefficient
β	parameter in strain hardening law

δ_{mouth}	crack mouth opening
δ_{tip}	crack tip opening
ε	permittivity of the solution
ε_f	crack tip film strain
ε_{ct}	plastic strain distribution for an advancing crack
$\dot{\varepsilon}_f$, $\dot{\varepsilon}_{ct}$	crack tip strain rate
λ	parameter in strain hardening law
λ	equivalent conductivity
μ	dynamic viscosity
ν	Poisson's ratio
ρ	material density
ρ_w	water density
σ_y	yield strength
ϕ_M^0	electrode potential of the material

Abbreviations

BOC	beginning of cycle
BWR	boiling water reactor
CGR	crack growth rate(s)
CPR	crack propagation rate(s)
CR	cold rolled
CT	compact tension
CW	cold work
dpa	displacement per atom
EOC	end of cycle
HR	hydrogen reaction
IASCC	irradiation assisted stress corrosion cracking
IGSCC	intergranular stress corrosion cracking
OR	oxygen reaction
PE	plane strain
PS	plane stress
PWR	pressurized water reactor
SA	solution annealed
SD	slip dissolution
SCC	stress corrosion cracking
TGSCC	transgranular stress corrosion cracking
WR	warm rolled

1 Introduction

The lifetime of some pressurized water reactor components can be limited because of stress corrosion cracking. Hence, research into the modelling of the crack growth rate in stainless steel is very important. Crack growth rate modelling software, CGR-1, was developed as part of the EU's FP6 project PERFECT by VUB in collaboration with SCK•CEN.
The first section in this thesis will tackle some general aspects with respect to stress corrosion cracking. This includes a brief description of crack propagation mechanisms.
Secondly, a comprehensive mathematical derivation of the slip dissolution/film rupture model will be provided. This model is the foundation in the software code of CGR-1. A discussion on the implementation of environmental, mechanical and material properties in the software is therefore discussed in the third chapter.
A calibration procedure of CGR-1 at the reference temperature of 320°C and at variable temperatures is also intensively discussed.
Some important comments regarding the crack tip strain rate conditions in the considered specimen is described.
Changes in crack growth rates will be studied by altering several input parameters like the environmental conditions, the material properties and the crack geometry. This subject is referred to as trend calculations with CGR-1.
The last part of the thesis consists of a list of suggestions and recommendations to the programmers of the CGR-1 software.
This will be followed by some general conclusions and closure remarks.

2 Stress corrosion cracking

2.1 Introduction

Stress corrosion cracking (SCC) is observed in engineering materials [1-2] that are subjected to (tensile) stresses in a corrosive environment. SCC is therefore also referred to as environmentally assisted cracking. Irradiation assisted stress corrosion cracking (IASCC) can be defined similarly, with the sole difference that effects due to irradiation must be included. The combined and synergetic interaction of mechanical and chemical forces results in slowly propagating cracks in the material. Knowledge on crack propagation rates is important because it will provide information on the lifetime of the component.
SCC and IASCC are represented schematically in Figure 2-1 which shows how the interaction between material, environment, stresses and radiation can lead to various phenomena that influence the mechanical, electrochemical, microstructural... properties of the material.

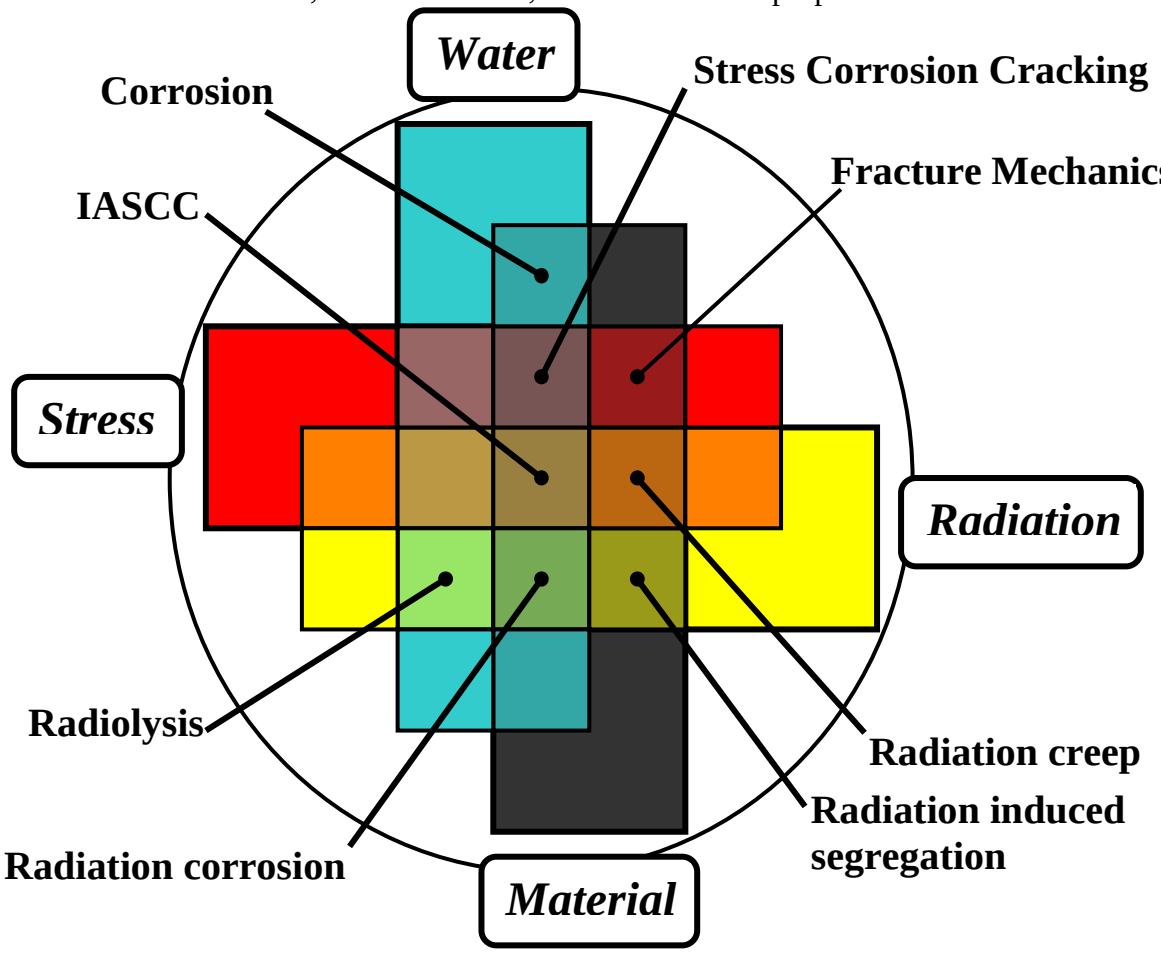

Figure 2-1: Interactions between material, radiation, environment and stresses

The generated cracks can grow along the grain boundaries or through the grains of the material. The former is known as intergranular stress corrosion cracking (IGSCC), the latter as transgranular stress corrosion cracking (TGSCC).
The nominal stresses encountered in SCC processes are relatively small, for instance compared to yield stresses, and can originate from externally applied or residual stresses that are considered to be static. When cyclic stresses are applied, one usually speaks about corrosion fatigue.

This section will introduce some aspects of the stress corrosion cracking process and the factors that influence this phenomenon. Furthermore, an overview of mechanisms that are considered to be responsible for SCC will be given.

2.2 The Stress corrosion cracking process

2.2.1 Introduction

The processes leading to failure due to stress corrosion cracking can be distinguished in three successive steps: crack initiation, crack propagation and final failure.
The research on crack initiation and propagation mechanisms is more important because these processes proceed very slowly compared to final rupture, implying that one of these will be the rate determining step. Indications of crack initiation or propagation are a signal for dedicated follow-up of the integrity of the structure.

2.2.2 Crack initiation

Several features have been identified as crack initiation sites, for instance the existence of flaws or small cracks at the surface introduced during fabrication, processing, manufacturing…
Other potential initiation sites are corrosion pits that were formed during exposure to a corrosive environment. Pitting corrosion or induced flaws do not always lead to cracking because this is also dependent on stress and strain at the tip, temperature, electrochemistry, fluid flow properties…
Intergranular attack due to sensitization or grain boundary segregation of phosphorus, sulphur, silicon… is also known to act as a crack initiation site. The most important consequence of these processes is that the chemical composition in the grain boundary changes, with respect to the bulk material, and becomes therefore more susceptible to corrosion. The grain boundaries are depleted in chromium and therefore lose their stainless character.
It is very difficult to measure crack initiation experimentally. Moreover, the term crack initiation is not well defined and it is difficult to determine when a pit becomes a crack or when intergranular corrosion becomes IGSCC. That is why one usually makes the assumption that there is a hypothetical crack present in the material when dealing with SCC problems. This is obviously a conservative approach from a safety point-of-view.
The phenomenon of crack initiation will not be further dealt with.

2.2.3 Crack propagation

Crack propagation is the logical successive step after initiation, but this is not always the case. Again, a conservative approach is preferable and it is tacitly assumed that every initiated crack will propagate sooner or later. Crack propagation rates can be experimentally investigated and have been mathematically modelled, in contrast to initiation. Crack propagation rates in SCC processes or usually of the order of 10^{-9} to 10^{-12}m/s, which means that they can be followed in time. Prediction of crack propagation rates is the subject of this thesis.

2.2.4 Final failure

When crack propagation has progressed to such extent that final rupture, which can be brittle or ductile, can not be prevented in a safewise manner and the mechanical integrity of the component is no longer guaranteed. Sudden brittle ruptures are usually very fast (~speed of sound) and can not be stopped once started. This process will not be discussed in this thesis.

2.3 Environmental factors

2.3.1 Introduction

The corrosive environment that is responsible for stress corrosion cracking has several properties that influence crack initiation and propagation. These properties include corrosion potential, pH, temperature, presence of impurities or dissolved species… One of the most important dissolved species, which is known to have an influence on SCC, is hydrogen.
In this part, the thermodynamic requirements for SCC and the kinetics of SCC will be qualitatively and briefly summarized. Finally, the phenomenon of hydrogen embrittlement will be introduced.

2.3.2 Thermodynamics of SCC

Crack growth in SCC processes can be related to the anodic dissolution rate of metal ions in the environment. A first requirement for SCC is therefore that dissolution in the electrolyte must be thermodynamically possible. Another requirement is the thermodynamical stability of an oxide or salt layer at the material-environment interface, for example Cr_2O_3 on stainless steels.
These requirements are represented in the environment by the electrode potential in the solution E.
Potential-pH diagrams (Pourbaix-diagrams) are also used to assess whether a material is thermodynamically susceptible to corrosion or not. These diagrams indicate what the thermodynamical stable form of the material is, given a couple E and pH. It should be mentioned that these diagrams are temperature dependent and are therefore only valid at one specific temperature.
Lack of availability of E-pH diagrams for various chemical environments and temperatures limits their applicability. Moreover, the chemistry and electrode potential in a crack, especially at the crack tip, may seriously differ from that in the bulk solution.
This consideration necessitates therefore other approaches.

2.3.3 Kinetics of SCC

Kinetics of SCC must be studied because estimated crack propagation rates in a corrosive environment may be so slow that they are acceptable. The same factors that were mentioned concerning thermodynamics (e.g. temperature, potential, pH…) also influence the SCC kinetics. Polarisation curves indicate at which rate (as current densities) the metal will corrode, given a certain potential.
The reaction rates are usually expressed using Faraday's law, namely the crack propagation rate is proportional to the average current density of the dissolved charged species at the crack tip. The conditions (stresses and strains, chemistry, electrochemistry…) at the crack tip are considered to be crucial for the determination of propagation rates, but those are very difficult to measure experimentally as the crack width is in the order of microns.
It is generally believed that a major rate limiting factor in growth rates is the transport of species in and out of the crack. This transport is influenced by crack geometry, dissolution rates at the crack walls, diffusion…

2.3.4 Hydrogen embrittlement

Hydrogen embrittlement explains stress corrosion cracking by hydrogen-induced subcritical crack growth. The hydrogen cations can be created by the consumption of electrons in a cathodic reaction. The atomic hydrogen diffuses easily in the material along the grain boundaries, especially if impurities (sulphur, phosphorous, tin…) are segregated in those

grain boundaries. The absorbed hydrogen causes enhanced embrittlement and a preferential pathway for crack propagation.

2.4 Material-related factors

2.4.1 Introduction

The influence of material properties is very complicated and is mainly related to the chemistry of the alloy and its microstructure. IGSCC, for example, has been observed in stainless steel with a high degree of sensitization, which is usually preceded by a change in chemistry at the grain boundaries.

2.4.2 Intergranular stress corrosion cracking

In general, two mechanisms are known to lead to IGSCC: grain boundary precipitation and grain boundary segregation.
Grain boundary precipitation in stainless steels is a process in which chromium forms carbide particles and diffuse to the grain boundary at elevated temperatures (500-850°C). This leads to a difference in chemical composition between the bulk material and the grain boundary. In a region adjacent to the grain boundary, the material is depleted in chromium and may therefore lose its stainless characteristic. This process is usually referred to as sensitization and is also influenced by the presence of molybdenum, nickel, silicon, manganese...
Grain boundary segregation has been observed when impurities like phosphorous, silicon and nitrogen are present on the grain boundary. Like in grain boundary precipitation, segregation alters the local chemistry, compared to the bulk alloy. The segregation of elements like phosphorous, nickel, iron and chromium on the grain boundary due to neutron irradiation, which is called radiation induced segregation, is an important process in intergranular IASCC.

2.4.3 Transgranular stress corrosion cracking

The occurrence of TGSCC is influenced by several material properties, like composition, dislocation distribution, geometry and density, microstructure, crystal structure…
The slip planarity and the role of impurities have a considerable effect on TGSCC. Transgranular corrosion occurs quite often along a plane with a high dislocation density created by planar slip. This mechanism is again influenced by the presence of impurities and their reactivity with environment.

2.5 Mechanical factors

The last contribution to the phenomenon of stress corrosion cracking is delivered by the mechanical properties of the material undergoing SCC. In this phenomenon, crack tip stress, crack tip strain rate and local stress intensity are key parameters in crack propagation rates. Nevertheless, different SCC mechanisms propose other mechanical factors as the rate determining one.
Most SCC tests are carried out with tensile stress perpendicular[1] to the existing crack, although the actual cracks are exposed to a complex combination of shear and tensile stresses. Usually, materials have a certain threshold stress under which no cracking behaviour is seen. It is known that mode 1 loading shows the lowest threshold stresses compared to other loading modes. This threshold stress can be explained by the observation that the passive film does not rupture at all and gives rise to threshold strain rates and threshold stress intensities. Once this film has ruptured, by chemical or mechanical action, the material repassivates and the repassivation rate will influence the velocity of the growing crack.

[1] The perpendicular loading is defined as mode 1 loading.

2.6 Crack propagation mechanisms

2.6.1 Introduction

Several crack propagation mechanisms have been developed [2] and they can mainly be distinguished in dissolution models and mechanical fracture models. Dissolution models explain crack propagation rates as preferential anodic dissolution at the advancing crack tip. Mechanical fracture models predict that concentrated mechanical stresses and strains at the crack tip cause material rupture without environmental interaction. There is, however, no international agreement on the precise mechanism and it is believed that SCC is achieved by the combination of two or more of the proposed models. Moreover, some models are shown to be valid for IGSCC and not for TGSCC and vice versa.
It has also been observed in experiments that crack growth velocities are not constant due to the presence of crack arrest markings, and models should be in agreement with this phenomenon as well. This section is merely a brief summary from [2] and pinpoints out some general ideas with respect to these important phenomena.

2.6.2 Dissolution models

2.6.2.1 Film rupture

The film rupture/repassivation mechanism or slip dissolution model is used in the CGR-1 (Crack Growth Rate - 1) software code and will be introduced and extensively discussed in the next chapter.
In short, this model is based on crack propagation by the mechanical rupture of the protective film, followed by the dissolution of bare metal exposed to the corrosive environment and the simultaneous renewal of the passivating film.

2.6.2.2 Active path intergranular stress corrosion cracking

The active path IGSCC model is based on the activity of the chemical species in the grain boundaries of the material. In this model, grain boundary segregation and precipitation are responsible for IGSCC. As mentioned before, these processes alter the local chemical composition at grain boundaries. The crack propagation rates are predicted by Faraday's law.

2.6.3 Mechanical fracture models

2.6.3.1 Corrosion tunnel

Emerging slip steps in the material create very small tunnels of atomic diameters that grow due to their interaction with the environment. Finally, final rupture is obtained by ductile fracture in the remaining ligaments. This model has been adapted according to experimental observations because the tunnels were actually identified as slots rather than tunnels.

2.6.3.2 Adsorption-enhanced plasticity

Adsorption of chemical species could cause hydrogen embrittlement, liquid metal embrittlement and SCC. In all these processes, the adsorbed species enhance the nucleation of dislocations at the crack tip. This increases the dislocation density and consequently the brittleness at the crack tip. As in the corrosion tunnel model, final rupture is caused by shear stresses at remaining ligaments.
Another model which explains SCC due to adsorption of dissolved species is the adsorption-induced brittle fracture model[2]. In this model, however, the species lower both the interatomic

[2] This model is also referred to as the Stress-Sorption model

bond strength in the metal and the stress required for cleavage fracture. The model predicts a continuous propagating crack which is in disagreement with experimental observations.

2.6.3.3 Tarnish rupture

In this model, the brittle passive surface film ruptures due to chemical or mechanical interaction, after which the bare metal reacts with the environment and the surface film is repaired, similar to the film rupture/repassivation model. IGSCC is explained by the observation that the oxide film penetrates into grain boundary ahead of the crack tip.

2.6.3.4 Film induced cleavage

This model explains crack propagation as follows: a small crack is initiated in the brittle oxide layer, crosses the oxide/metal interface and continues to grow in the metal where the crack velocity decreases and finally the crack arrests. After thorough investigation it has been pointed out that a brittle crack can propagate in a ductile matrix if it is sharp and if the crack velocity in the surface layer is high enough.

2.7 Conclusion

Several different mechanisms have been proposed to describe stress corrosion cracking, but still a lot of research is required to expand and improve the knowledge on this phenomenon. The understanding of the different complicated synergistic interactions between stresses, material properties and the environment is quite well established but needs further improvement. The need for mechanistic crack propagation modelling is considered to be very useful because dedicated experiments are expensive, difficult and time consuming. These experiments are nevertheless necessary to verify the validity of the developed models.

3 The film rupture/repassivation model

3.1 Introduction

The film rupture/repassivation model is the basic model used in CGR-1 to assess crack propagation rates. This slip dissolution model has been developed by Ford and Andresen [3-4] and has proven its performance in calculating velocities of propagating cracks. In the first part of this section, a mathematical development of this model will be provided. In the second part, a description for the plane strain and plane stress crack tip strain rate will be given because the crack tip strain rate is a crucial parameter in the slip dissolution (SD) model. Some additional adjustments to the original model will be given to correspond with the expressions that will be used in the CGR-1 software. Figure 3-1 gives a visual representation of the crack acting as interface between the material and the environment.

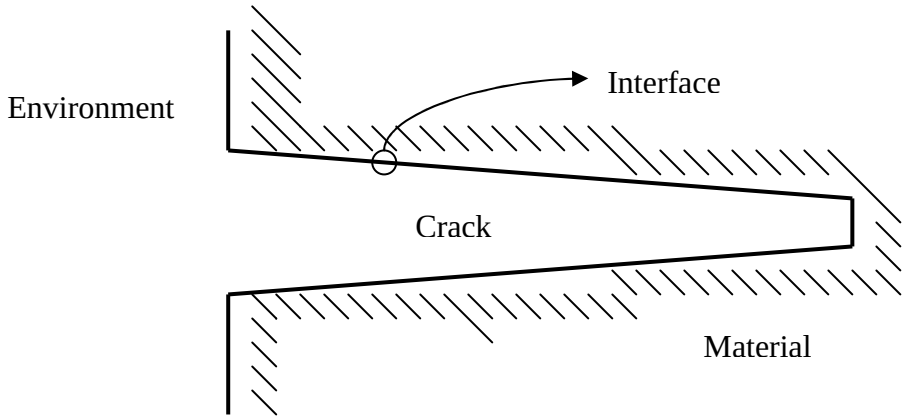

Figure 3-1: Representation of the crack as interface between the environment and the material

3.2 The slip dissolution model

3.2.1 Introduction

In the slip dissolution model, the oxide film that protects the metal from corrosion is ruptured at a certain time. The bare metal that is exposed to the environment starts to dissolve immediately because an electrochemical anode is created. The metallic cations that are dissolved start to migrate through the crack, while the electrons generated by the anodic reaction travel through the metallic lattice and are consumed by cathodic reactions somewhere at the material/environment interface. The migration of the cations through the crack is achieved by the means of diffusion, ionic migration and convection. Mass and electroneutrality conservation within the entire crack is required.
During the time that the metal dissolves, the passive oxide layer is being repaired slowly at the sites where it previously was destroyed. This continues until the layer is completely renewed and covers the entire metal surface in the crack tip region. The whole process is repeated and the crack propagation rate is therefore mainly determined by rate at which the surface repassivates and the number of ruptures per unit of time.

3.2.2 Mathematical derivation

The crack growth rate $\dot{a}$ [m/s] is equivalent to the dissolution rate at the bare surface of the crack tip. This dissolution rate is given by Faraday's law:

$$\dot{a} = \left(\frac{M}{F\rho z}\right)\left(\frac{Q_d}{t_f}\right) \tag{1}$$

where Q_d is the charge density [C/m²] exchanged during the period of film rupture t_f [s], M is the atomic weight [g/mol], F is Faraday's constant [C/mol], ρ is the density [kg/m³] and z the valence [-].
The current density i(t) [A/m²] caused by the dissolution of charged species at the crack tip during repassivation is schematically shown in Figure 3-2 and is modelled by the following expressions.

$$\begin{cases} i(t) = \hat{i}_0 \quad for \;\; 0 < t < t_0 \\ i(t) = \hat{i}_0 \left(\frac{t}{t_0}\right)^{-m} \quad for \;\; t_0 < t < t_f \end{cases} \tag{2}$$

In this expression, m is the repassivation parameter [-] or the current decay constant for repassivation.

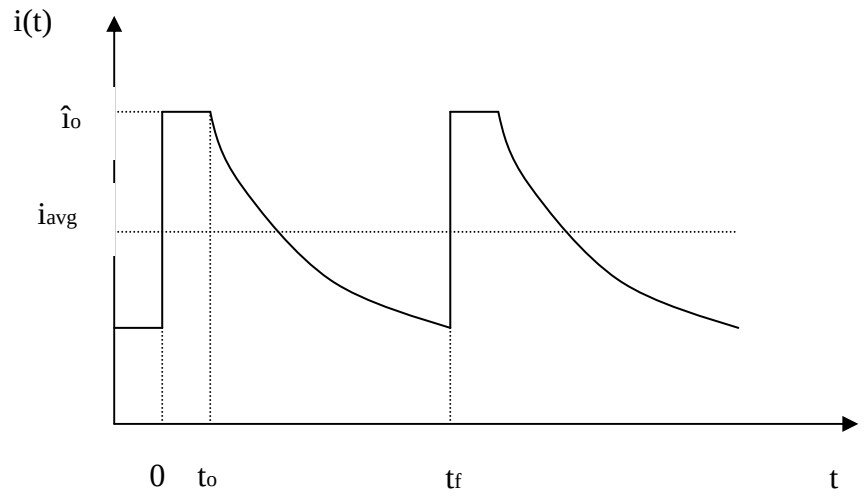

Figure 3-2: Current density profile at the crack tip

The charge density can be related to the current density by

$$Q_d = \int_0^{t_0} i(t)dt + \int_{t_0}^{t_f} i(t)dt \tag{3}$$

The very small period from 0 to t_0, at which a constant current density i_0 is present at the crack tip immediately after film rupture, is usually neglected ($t_0 \approx 0$). Therefore

$$Q_d = \hat{i}_0 {t_0}^m \int_0^{t_f} t^{-m} dt \tag{4}$$

To obtain the average current density during the process, the charge density must be evaluated over the entire time interval:

$$i_{avg} = \frac{\hat{i}_0 t_0{}^m \int_0^{t_f} t^{-m} dt}{\int_0^{t_f} dt} = \frac{Q_d}{t_f} \tag{5}$$

After performing the integration, one finds the following expression for the average current density at the crack tip:

$$i_{avg} = \frac{\hat{i}_0 t_0{}^m}{(1-m) t_f{}^m} \tag{6}$$

Combining equations (1) and (6) yields

$$\dot{a} = \left(\frac{M}{F \rho z} \right) \left(\frac{\hat{i}_0 t_0{}^m}{(1-m) t_f{}^m} \right) \tag{7}$$

The rupture period t_f is related to the rupture strain in the film, ε_f [-], and the crack tip strain rate, $\dot{\varepsilon}_{ct}$ [1/s], by

$$t_f = \frac{\varepsilon_f}{\dot{\varepsilon}_{ct}} \tag{8}$$

Inserting (8) into (7) gives then the following expression:

$$\dot{a} = \left(\frac{M}{F \rho z} \right) \left(\frac{\hat{i}_0 t_0{}^m}{(1-m) \varepsilon_f{}^m} \right) \dot{\varepsilon}_{ct}{}^m \tag{9}$$

According to [5], the average current density at the crack tip is a function of the potential difference between the material (ϕ_M^L) and the solution (ϕ_M^0).

$$i_{avg} \propto \exp\left(\frac{\phi_M^L - \phi_M^0}{b_a}\right) \quad \text{with} \quad b_a = \frac{RT}{\alpha_i n F} \tag{10}$$

R is the gas constant [J/Kmol], T is the absolute temperature [K], F is Faraday's constant [C/mol], α_i is the anodic transfer coefficient [-] for dissolution and n is the number of electrons involved [-].
Next, the electrode potential E_{tip} [V] at the crack tip is introduced as:

$$E_{tip} = \phi_M^L - \phi_M^0 \tag{11}$$

and equation (9) leads to the final formula for the crack growth rate:

$$\dot{a} = \left(\frac{M}{F \rho z} \right) \exp\left(\frac{\alpha F}{RT} E_{tip} \right) \left(\frac{\hat{i}_0 t_0{}^m}{(1-m) \varepsilon_f{}^m} \right) \dot{\varepsilon}_{ct}{}^m \tag{12}$$

where $\alpha = n.\alpha_i$

3.3 The crack tip strain rate

3.3.1 Introduction

One crucial factor in equation (12) is the crack tip strain rate because it is a function of the crack growth rate. This means that there is no immediate closed analytical formulation for the determination of the actual crack growth rate. Shoji and his co-workers [67] have developed analytical expressions for the crack tip strain rate. Two different expressions for the crack tip strain rate are derived hereunder: one for plane strain and one for plane stress.

3.3.2 Plane strain crack tip strain rate

The development of the plane strain crack tip strain rate formula starts with the expression for the plastic strain distribution ε_{ct} for a moving crack as derived by Gao and Kwang [8]:

$$\varepsilon_{ct} = \beta\left(\frac{\sigma_y}{E}\right)\left\{\ln\left[\left(\frac{\lambda}{r}\right)\left(\frac{K}{\sigma_y}\right)^2\right]\right\}^{\frac{n}{n-1}} \tag{13}$$

Here, β and λ are dimensionless constants, K is the stress intensity factor [MPa√m], E is Young's modulus [MPa], σ_y is the yield strength [MPa], n is the Ramberg-Osgood work hardening exponent [-] and r is the distance ahead of the advancing crack tip [m].
To find an expression for the crack tip strain rate, the derivative of ε_{ct} with respect to time is taken with the application of the chain rule.

$$\dot{\varepsilon}_{ct} = \frac{d\varepsilon_{ct}}{dt} = \frac{d\varepsilon_{ct}}{dr}\frac{dr}{dt} \tag{14}$$

This is a useful expression because the latter derivative is related to the crack growth rate according to:

$$\frac{dr}{dt} = -\frac{da}{dt} = -\dot{a} \tag{15}$$

These mathematical manipulations finally result in:

$$\dot{\varepsilon}_{ct} = \beta\left(\frac{\sigma_y}{E}\right)\left(\frac{n}{n-1}\right)\left(\frac{1}{r}\right)\left\{\ln\left[\left(\frac{\lambda}{r}\right)\left(\frac{K}{\sigma_y}\right)^2\right]\right\}^{\frac{1}{n-1}}\dot{a} \tag{16}$$

To investigate the influence of the stress intensity rate or loading rate, a similar expression can be found by taking the derivative with respect to K:

$$\frac{d\varepsilon_{ct}}{dt} = \frac{d\varepsilon_{ct}}{dK}\frac{dK}{dt} = \frac{d\varepsilon_{ct}}{dK}\dot{K} \tag{17}$$

resulting in:

$$\dot{\varepsilon}_{ct} = \beta\left(\frac{\sigma_y}{E}\right)\left(\frac{n}{n-1}\right)\left(\frac{2\dot{K}}{K}\right)\left\{\ln\left[\left(\frac{\lambda}{r}\right)\left(\frac{K}{\sigma_y}\right)^2\right]\right\}^{\frac{1}{n-1}} \tag{18}$$

The use of these manipulations tacitly assumes that the stress intensity factor K is independent of the distance r ahead of the growing crack. Moreover, no factors in expression (13), other than r and K may have any time dependency.
The combination of expressions (16) and (18) yields to:

$$\dot{\varepsilon}_{ct} = \beta\left(\frac{\sigma_y}{E}\right)\left(\frac{n}{n-1}\right)\left\{\ln\left[\left(\frac{\lambda}{r}\right)\left(\frac{K}{\sigma_y}\right)^2\right]\right\}^{\frac{1}{n-1}}\left(\frac{2\dot{K}}{K}+\frac{\dot{a}}{r}\right) \tag{19}$$

When the plastic zone size Rp [m], given by:

$$Rp = \lambda\left(\frac{K}{\sigma_y}\right)^2 \tag{20}$$

is introduced, equation (19) reduces to:

$$\dot{\varepsilon}_{ct} = \beta\left(\frac{\sigma_y}{E}\right)\left(\frac{n}{n-1}\right)\left(\ln\frac{Rp}{r}\right)^{\frac{1}{n-1}}\left(\frac{2\dot{K}}{K}+\frac{\dot{a}}{r}\right) \tag{21}$$

3.3.3 Plane stress crack tip strain rate

A similar expression as (13) can be found for the plastic strain distribution for an advancing crack [9], but now under plane stress conditions:

$$\varepsilon_{ct} = \beta\left(\frac{\sigma_y}{E}\right)\left\{\ln\left[\left(\frac{\lambda}{r}\right)\left(\frac{K}{\sigma_y}\right)^2\right]+\frac{1}{2}\ln\left[\left(\frac{\lambda}{r}\right)\left(\frac{K}{\sigma_y}\right)^2\right]^2\right\}^{\frac{n}{n-1}} \tag{22}$$

The parameters that appear in this expression are the same as in (13), but the expression is somewhat more complex. The derivation of the plane stress crack tip strain rate is completely analogous to the previous procedure. First, the derivative of ε_{ct} with respect to time is taken with the application of the chain rule.

$$\dot{\varepsilon}_{ct} = \frac{d\varepsilon_{ct}}{dt} = \frac{d\varepsilon_{ct}}{dr}\frac{dr}{dt} \tag{14}$$

The crack propagation rate can be recognized as:

$$\frac{dr}{dt} = -\frac{da}{dt} = -\dot{a} \tag{15}$$

and expression (22) becomes

$$\dot{\varepsilon}_{ct} = \beta\left(\frac{\sigma_y}{E}\right)\left(\frac{n}{n-1}\right)\left\{\ln\left[\left(\frac{\lambda}{r}\right)\left(\frac{K}{\sigma_y}\right)^2\right]+\frac{1}{2}\ln\left[\left(\frac{\lambda}{r}\right)\left(\frac{K}{\sigma_y}\right)^2\right]^2\right\}^{\frac{1}{n-1}}\left(1+\ln\left[\left(\frac{\lambda}{r}\right)\left(\frac{K}{\sigma_y}\right)^2\right]\right)\frac{\dot{a}}{r} \tag{23}$$

The influence of stress intensity rate can be examined by taking as before the time derivative with respect to time of expression (22):

$$\frac{d\varepsilon_{ct}}{dt} = \frac{d\varepsilon_{ct}}{dK}\frac{dK}{dt} = \frac{d\varepsilon_{ct}}{dK}\dot{K} \tag{17}$$

and this results in:

$$\dot{\varepsilon}_{ct} = \beta\left(\frac{\sigma_y}{E}\right)\left(\frac{n}{n-1}\right)\left\{\ln\left[\left(\frac{\lambda}{r}\right)\left(\frac{K}{\sigma_y}\right)^2\right] + \frac{1}{2}\ln\left[\left(\frac{\lambda}{r}\right)\left(\frac{K}{\sigma_y}\right)^2\right]^2\right\}^{\frac{1}{n-1}}\left(1+\ln\left[\left(\frac{\lambda}{r}\right)\left(\frac{K}{\sigma_y}\right)^2\right]\right)\frac{2\dot{K}}{K} \qquad (24)$$

The combination of expressions (23) and (24) leads to the final expression for the plane stress crack tip strain rate. It is assumed that all factors, except r and K, are time independent and that K and r are independent of each other.

$$\dot{\varepsilon}_{ct} = \beta\left(\frac{\sigma_y}{E}\right)\left(\frac{n}{n-1}\right)\left\{\ln\left[\left(\frac{\lambda}{r}\right)\left(\frac{K}{\sigma_y}\right)^2\right] + \frac{1}{2}\ln\left[\left(\frac{\lambda}{r}\right)\left(\frac{K}{\sigma_y}\right)^2\right]^2\right\}^{\frac{1}{n-1}}\left(1+\ln\left[\left(\frac{\lambda}{r}\right)\left(\frac{K}{\sigma_y}\right)^2\right]\right)\left(\frac{2\dot{K}}{K}+\frac{\dot{a}}{r}\right) \qquad (25)$$

Again, the plastic zone size can be introduced in equation (25), which results in:

$$\dot{\varepsilon}_{ct} = \beta\left(\frac{\sigma_y}{E}\right)\left(\frac{n}{n-1}\right)\left[\ln\frac{Rp}{r} + \frac{1}{2}\left(\ln\frac{Rp}{r}\right)^2\right]^{\frac{1}{n-1}}\left[1+\ln\left(\frac{Rp}{r}\right)\right]\left(\frac{2\dot{K}}{K}+\frac{\dot{a}}{r}\right) \qquad (26)$$

4 CGR-1

4.1 Introduction

CGR-1 is a software tool for mechanistic modelling of crack propagation rates in type 316 stainless steels in pressurized water reactor relevant conditions. The software code has been developed as a part of the EU FP6 project PERFECT by VUB (Vrije Universiteit Brussel) in collaboration with the SCK•CEN (The Belgian Nuclear Research Centre).
The code is mainly based on two computation methods: finite element based modelling of the environment (E_{tip}[3]) and an analytical expression for the crack tip strain rate $\left(\dot{\varepsilon}_{ct}\right)$[4].

The crack tip electrode potential E_{tip} and the crack tip strain rate are the crucial parameters in the slip dissolution model.

4.2 Slip dissolution and crack tip strain rate

4.2.1 Introduction

The mathematical derivation of the slip dissolution mechanism and the crack tip strain rate equation was given in the previous chapter. This section does not want to repeat all those calculations, but rather wants to present how the expressions are programmed in the actual CGR-1 software code.

4.2.2 The analytical model

Faraday's law is postulated as an expression which relates the average current density at the crack tip with the crack propagation rate.

$$\dot{a} = \frac{M i_{avg}}{F \rho z} \tag{27}$$

The slip dissolution model provides a relation between the potential at the tip, the crack tip strain rate and the average current density.

$$i_{avg} = \hat{i}_0 \exp\left(\frac{\alpha F}{RT} E_{tip}\right)\left(\frac{t_0^{\ m}}{(1-m)\varepsilon_f^{\ m}}\right)\dot{\varepsilon}_{ct}^{\ m} \tag{28}$$

The analytical expression for the plane stress crack tip strain rate that was derived in the previous chapter is repeated hereunder.

$$\dot{\varepsilon}_{ct} = \beta\left(\frac{\sigma_y}{E}\right)\left(\frac{n}{n-1}\right)\left[\ln\frac{Rp}{r} + \frac{1}{2}\left(\ln\frac{Rp}{r}\right)^2\right]^{\frac{1}{n-1}}\left[1+\ln\frac{Rp}{r}\right]\left(\frac{2\dot{K}}{K} + \frac{\dot{a}}{r}\right) \tag{26}$$

Formula (28) is very important because it clearly shows the dependency of the crack propagation rate, or the current density as they are related to each other by Faraday's law, on other parameters. Most of these parameters are constants for the considered system and a list of those is provided in Table 4-1, while other factors are input parameters in the user interface and are given in Table 4-2 together with their input ranges. The parameter $\hat{i}_0$ is the sensitization factor and expresses the activity of the grain boundaries. This activity is related

[3] See equation (12)
[4] See equation (21) and (26)

to the maximum dissolution rate, or current density, at the moment of film rupture as shown in Figure 3-2.
More important is the presence of the crack tip strain rate and the electrode potential in this expression.
Expression (26) has the major difficulty that the strain rate at the crack tip is a function of the loading rate and, more important, the crack propagation rate. This means that there is no straightforward expression that directly relates the crack propagation rate to the crack tip strain rate. This problem is circumvented in CGR-1 by assuming that the stress intensity factor at the crack tip is constant and that the loading rate is therefore equal to zero ($\dot{K} = 0$), which modifies expression (26):

$$\dot{\varepsilon}_{ct} = \beta\left(\frac{\sigma_y}{E}\right)\left(\frac{n}{n-1}\right)\left[\ln\frac{Rp}{r} + \frac{1}{2}\left(\ln\frac{Rp}{r}\right)^2\right]^{\frac{1}{n-1}}\left[1+\ln\frac{Rp}{r}\right]\frac{\dot{a}}{r} \tag{29}$$

All factors in expression (29) except $\dot{a}$ are constants. The ratio of the crack tip strain rate to the crack propagation rate is fixed for a given input matrix and is introduced as G. The combination of (27), (28) and (29) gives the final equation for the current density calculation in the software code.

$$i_{avg} = \left[\hat{i}_0 \exp\left(\frac{\alpha F}{RT} Etip\right)\frac{1}{(1-m)}\left(\frac{t_0}{\varepsilon_f}\frac{M}{\rho z F} G\right)^m\right]^{\frac{1}{1-m}} \tag{30}$$

Parameter	Symbol	Value	Unit
Atomic weight	M	0.055847	kg/mol
Material density	ρ	7860	kg/m³
Charge	z	2	-
Faraday's constant	F	96500	C/mol
Anodic transfer coefficent	α	0.5	-
Universal gas constant	R	8.31441	J/mol.K
Bare surface exposure time	t_0	0.1	s
Film strain	ε_f	0.0001	-
Parameter in strain hardening law	β	5.08	-
Plastic zone size constant	λ	0.3	-
Distance ahead of crack tip	r	0.19	mm

Table 4-1: Table of constants used in CGR-1

The electrode potential at the crack tip E_{tip} is the only factor in the expressions that has not been discussed yet. A value for E_{tip} is not obtained by analytical means, but is calculated by a finite element based method that models the environment and that will be discussed in the following section[5].

[5] This discussion will introduce additional input parameters, constants and formulas. The input parameters are already included in Table 3-2.

Parameter	Symbol	Range	Unit
Stress intensity	K	[10-50]	MPa√m
Young's modulus	E	[150-300]	GPa
Poisson's ratio	υ	[0.25-0.35]	-
Yield strength	σ_y	[100-1000]	MPa
Sensitization factor	i_0	[0.01-100]	-
Repassivation parameter	m	[0.1-0.9]	-
Strain hardening exponent	n	[2-15]	-
Crack length	L	[1-10]	mm
Boric acid concentration	B	[0-5000]	ppm
Lithium hydroxide concentration	Li	[0-10]	ppm
Dissolved hydrogen concentration	H_2	[0-50]	cc/kg
Dissolved oxygen concentration	O_2	[0-5000]	ppm
Temperature	T	[25-350]	°C
Reynolds number	Re	[0-2000]	-

Table 4-2: Table of input parameters used in CGR-1

4.3 The environment

4.3.1 Introduction

The finite element calculation models the environment and will provide a value for the crack tip electrode potential, necessary for the final result: the determination of the crack propagation rate. This section covers an explanation of the manner how the crack geometry, fluid flow conditions and chemical/electrochemical variables are calculated. Apart from the potential at the crack tip, other variables like pH, concentrations of dissolved species, fluid flow properties and the electrode potential all along the material/environment interface can be obtained.

4.3.2 Crack geometry

The design of the crack can be changed by altering the crack length. According to [10], the crack mouth opening δ_{mouth} [μm] and the crack tip opening δ_{tip} [μm] are function of material properties and the crack length L [mm]according to the following expressions:

$$\delta_{tip}\,[m] = 0.6\left(1-\nu^2\right)\frac{K\,[MPa\sqrt{m}]^2}{E\,[MPa]\sigma_y\,[MPa]} \tag{31}$$

$$\delta_{mouth}\,[\mu m] = \delta_{tip}\,[\mu m] + 6.803.10^{-4}\,K\,[MPa\sqrt{m}]E\,[GPa]L\,[mm] \tag{32}$$

In this equation, ν is the Poisson's ratio [-], K is the stress intensity factor, E is Young's modulus, σ_y is the yield strength and L is the crack length. All these parameters are input variables and their input ranges can be found in Table 4-2.
2D and 3D representations of this geometry are shown in Figure 4-1 and Figure 3-2, respectively. It should be mentioned that CGR-1 is in a 2D geometry and the 3D representation is only illustrative.

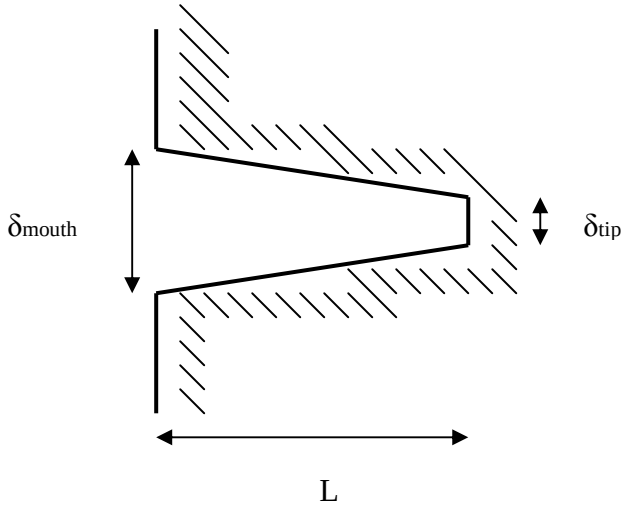

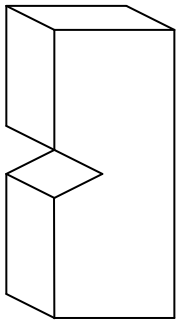

Figure 4-1: 2D representation of crack geometry **Figure 4-2: 3D representation of crack geometry**

4.3.3 Fluid flow

The fluid flow in the system is modelled using the incompressible Navier-Stokes equation and the continuity equation.

$$\rho_w\left(\frac{\partial\vec{v}}{\partial t}+\left(\vec{v}.\vec{\nabla}\right).\vec{v}\right)=\mu\vec{\nabla}^2\vec{v}-\vec{\nabla}p \tag{33}$$

$$\vec{\nabla}.\vec{v}=0 \tag{34}$$

In these expressions, v is the fluid velocity [m/s], p is the hydrostatic pressure [Pa], ρ_w is the water density [kg/m³] and μ is the dynamic viscosity [kg/m.s] of the fluid. The fluid density and dynamic viscosity are temperature dependent and are calculated by the following expressions with the temperature expressed in Kelvin [11]:

$$\rho_w=981.69673+0.526983113(T-273.15)-1.0159986.10^{-2}(T-273.15)^2$$
$$+3.49002924.10^{-5}(T-273.15)^3-5.638283345.10^{-8}(T-273.15)^4 \tag{35}$$

$$\mu=0.1167(T-245)^{-1,2383} \tag{36}$$

Equations (33) and (34) form a system of two equations with two unknowns, i.e., pressure and fluid velocity. The temperature is an input variable, so density and viscosity are fixed for every specific case and the fluid velocity and pressure can be calculated at any point of the system if a boundary condition is provided.
This is achieved through a predetermined inlet flow condition by the Reynolds number [-], which is an input parameter, as can be seen in Table 4-2.

$$\mathrm{Re}=\frac{\rho_w vL}{\mu} \tag{37}$$

The units for the density ρ_w, fluid velocity v and dynamic viscosity μ are the same as before. The characteristic length L, here the width of the central channel[6], is fixed at 5mm.

[6] This is not the length of the crack

4.3.4 Chemistry/Electrochemistry

The transport of charged and dissolved species in the environment is modelled using dilute solution theory [12]. The first formula for the modelling of the ionic transport is the Nernst-Planck equation.

$$\vec{N}_i = -D_i \vec{\nabla} C_i - \frac{F}{RT} z_i D_i C_i \vec{\nabla} U + C_i \vec{v} \tag{38}$$

$\vec{N}_i$ [mol/m²s] is the flux of all "i" species in the environment. The first term in the equation accounts for diffusive transport, according to Fick's law, with D_i [m²/s] the respective diffusion coefficients for all "i" species and C_i [mol/m³] their concentration in the system. The diffusion coefficients of the species are provided in Table 4-3.
The second term is the electro-migration term and is an additional term for transport of the charged species in the system. U [V] is the solution potential, z_i is the charge for all i species and F, R, T, D_i and C_i have been defined before.
The last term in equation (38) takes into account transport by convection. The fluid velocity is already fixed at every point by the expressions in the previous section.
Throughout the whole system, conservation of mass requires:

$$\frac{\partial C_i}{\partial t} = -\vec{\nabla} \vec{N}_i + \sum_k R_{k,i} \tag{39}$$

In this expression, $R_{k,i}$ is the production term for all species in reaction k.
Equations (38) and (39) constitute a system of "n" equations for all "i" species, which is not enough because the solution potential U is also unknown.
An additional expression is therefore provided by the Poisson equation:

$$\nabla^2 U = -\frac{F}{\varepsilon} \sum_{i=1}^{n} z_i C_i \tag{40}$$

where ε [C²/Nm²] is the permittivity of the solution. With these equations, all concentrations of all i species and the solution potential can be calculated. This will yield the electrode potential at the entire material/environment interface and a value for E_{tip}, the only factor still missing in expression (30).

4.3.5 Homogeneous reactions

Boric acid, $B(OH)_3$, is added to the primary loop of a PWR to control the reactivity of the reactor core. The consequence is that the pH lowers significantly and corrosion of all materials is enhanced. Lithium hydroxide, Li(OH), is added to the primary circuit to stabilize the pH at preferential values. Both B and Li [ppm] concentrations are input parameters and subjected to the following homogeneous reactions [12]:

$$PWR1 \qquad B(OH)_3 + OH^- \underset{kPWR-1}{\overset{kPWR1}{\rightleftharpoons}} B(OH)_4^- \tag{41}$$

$$PWR2 \qquad B(OH)_4^- + B(OH)_3 \underset{kPWR-2}{\overset{kPWR2}{\rightleftharpoons}} B_2(OH)_7^- \tag{42}$$

$$PWR3 \qquad B_2(OH)_7^- + B(OH)_3 \underset{kPWR-3}{\overset{kPWR3}{\rightleftharpoons}} B_3(OH)_{10}^- \tag{43}$$

$$PWR4 \qquad Li^+ + OH^- \underset{kPWR-4}{\overset{kPWR4}{\rightleftharpoons}} LiOH \tag{44}$$

$$PWR5 \qquad Li^+ + B(OH)_4^- \underset{kPWR-5}{\overset{kPWR5}{\rightleftharpoons}} LiB(OH)_4 \tag{45}$$

Based on the pQ_i[7], which is temperature dependent, the Q_i for all species are calculated. This allows the calculation of P_i and the reaction rate constant $kPWR_i$ as:

$$\forall i \quad Q_i = 10^{pQ_i} \tag{46}$$

$$pQ_1 = \frac{1573.21}{T} + 28.6059 + 0.012078T - 13.2258\log_{10}(T) \tag{47}$$

$$pQ_2 = \frac{2756.1}{T} - 18.966 + 5.835\log_{10}(T) \tag{48}$$

$$pQ_3 = \frac{3339.5}{T} - 8.084 + 1.497\log_{10}(T) \tag{49}$$

$$pQ_4 = \log_{10}(1.99) \tag{50}$$

$$pQ_5 = \log_{10}(2.12) \tag{51}$$

$$P_2 = \frac{Q_2}{Q_1} \tag{52}$$

$$P_3 = \frac{Q_3}{Q_2} \tag{53}$$

$$kPWR1 = \frac{Q_1}{\rho} \tag{54}$$

$$kPWR2 = \frac{Q_2}{\rho} \tag{55}$$

$$kPWR3 = \frac{Q_3}{\rho} \tag{56}$$

$$kPWR4 = \frac{Q_4}{\rho} \tag{57}$$

$$kPWR5 = \frac{Q_5}{\rho} \tag{58}$$

Three additional homogeneous reactions are included: one for water dissociation and two for the hydrolysis of metal ions:

$$R17 \qquad H_2O \underset{k_{-17}}{\overset{k_{17}}{\rightleftharpoons}} H^+ + OH^- \tag{59}$$

$$R18 \qquad M^{2+} + H_2O \underset{k_{-18}}{\overset{k_{18}}{\rightleftharpoons}} MOH^+ + H^+ \tag{60}$$

$$R19 \qquad MOH^+ + H_2O \underset{k_{-19}}{\overset{k_{19}}{\rightleftharpoons}} M(OH)_2 \downarrow + H^+ \tag{61}$$

In these reactions, k_{18} and k_{19} are $1.01\ 10^5$ and k_{-18} and k_{-19} are equal to zero. For the water dissociation, the reaction rate constants are dependent on the density of the water and the temperature according to following expressions:

$$\begin{aligned} k_{-17} &= 6.62.10^{10} + 1.48.10^{9}(T - 273.15) + 1.28.10^{7}(T - 273.15)^2 \\ &-6.03.10^{4}(T - 273.15)^3 + 128(T - 273.15)^4 \end{aligned} \tag{62}$$

[7] The pQi, sometimes written as pK in the literature is related to Qi (or K) through expression (46) and Qi is the equilibrium constant for the reactions (41) to (45).

$$k_{17} = k_{-17} K_w \rho_w (T_f)^2 \tag{63}$$

$$T_f = 647.25 - T \ [K] \tag{64}$$

$$\rho_w = \frac{1 + 0.1342489 T_f^{1/3} - 3.946263.10^{3} T_f}{3.1975 + 0.3151548 T_f^{1/3} - 1.203374.10^{3} T_f + 7.489081.10^{-13} T_f^{4}} \tag{65}$$

$$K_w = 10^{pK_w} \ \ [mol/kg] \tag{66}$$

$$pK_w = -4.098 - \frac{3245.2}{T} + \frac{2.2363.10^{5}}{T^2} - \frac{3.9984.10^{7}}{T^3} + \left(13.957 - \frac{1262.3}{T} + \frac{8.5641.10^{5}}{T^2}\right) \log\left(\rho_w (T_f)\right) \tag{67}$$

4.3.6 Diffusion coefficients

The diffusion coefficients for the species considered in CGR-1 are provided in Table 4-3. In this table, the parameter λ is the equivalent conductivity [Scm²/equivalent] and is equal to the specific conductivity of a solution where 1g equivalent/dm³ solid material is dissolved. Obviously, this only needs to be done for the charged species. The value for the diffusion coefficient needs to be adjusted for temperature.

Species	Z	Dk based on	Temperature correction
H^+	+1	$\lambda^{298K} = 350 Scm^2 / equiv$	$D_k^T = \frac{1}{10}\frac{\lambda_k^{298K}}{z_i^2}\frac{\mu_{298K}}{\mu_T}\frac{T}{298}\frac{RT}{\rho_w F^2}$
OH^-	–1	$\lambda^{298K} = 199 Scm^2 / equiv$	$D_k^T = \frac{1}{10}\frac{\lambda_k^{298K}}{z_i^2}\frac{\mu_{298K}}{\mu_T}\frac{T}{298}\frac{RT}{\rho_w F^2}$
O_2	0	$0.000000803 \exp\left(\frac{-14600}{RT}\right) \quad [m^2/s]$	
H_2	0	$0.0001 \exp\left(-5.700267 - \frac{296.7439}{T} - \frac{288379.2}{T^2}\right) \quad [m^2/s]$	
H_2O	0	$D^{298K} = 1 \quad [m^2/s]$	$D_k^T = D_k^{298K}\frac{\mu_{298K}}{\mu_T}\frac{T}{298}$
$B(OH)_4^-$	–1	$\lambda^{298K} = 40 Scm^2 / equiv$	$D_k^T = \frac{1}{10}\frac{\lambda_k^{298K}}{z_i^2}\frac{\mu_{298K}}{\mu_T}\frac{T}{298}\frac{RT}{\rho_w F^2}$
$B(OH)_3$	0	$D^{298K} = 2.10^{-9} \quad [m^2/s]$	$D_k^T = D_k^{298K}\frac{\mu_{298K}}{\mu_T}\frac{T}{298}$
$B(OH)_7^-$	–1	$\lambda^{298K} = 34 Scm^2 / equiv$	$D_k^T = \frac{1}{10}\frac{\lambda_k^{298K}}{z_i^2}\frac{\mu_{298K}}{\mu_T}\frac{T}{298}\frac{RT}{\rho_w F^2}$
$B(OH)_{10}^-$	–1	$\lambda^{298K} = 27 Scm^2 / equiv$	$D_k^T = \frac{1}{10}\frac{\lambda_k^{298K}}{z_i^2}\frac{\mu_{298K}}{\mu_T}\frac{T}{298}\frac{RT}{\rho_w F^2}$
Li^+	+1	$\lambda^{298K} = 39 Scm^2 / equiv$	$D_k^T = \frac{1}{10}\frac{\lambda_k^{298K}}{z_i^2}\frac{\mu_{298K}}{\mu_T}\frac{T}{298}\frac{RT}{\rho_w F^2}$
$Li(OH)$	0	$D^{298K} = 2.10^{-9} \quad [m^2/s]$	$D_k^T = D_k^{298K}\frac{\mu_{298K}}{\mu_T}\frac{T}{298}$
$LiB(OH)_4$	0	$D^{298K} = 2.10^{-9} \quad [m^2/s]$	$D_k^T = D_k^{298K}\frac{\mu_{298K}}{\mu_T}\frac{T}{298}$
M^{2+}	+2	$\lambda^{298K} = 39 Scm^2 / equiv \quad cfr \ Li^+$	$D_k^T = \frac{1}{10}\frac{\lambda_k^{298K}}{z_i^2}\frac{\mu_{298K}}{\mu_T}\frac{T}{298}\frac{RT}{\rho_w F^2}$
$M(OH)^+$	+1	$\lambda^{298K} = 39 Scm^2 / equiv \quad cfr \ Li^+$	$D_k^T = \frac{1}{10}\frac{\lambda_k^{298K}}{z_i^2}\frac{\mu_{298K}}{\mu_T}\frac{T}{298}\frac{RT}{\rho_w F^2}$

Table 4-3: Diffusion coefficients used in CGR-1

4.3.7 Electrochemical reactions

The electrochemical reactions that are implemented are very regular anodic and cathodic reactions in an aqueous environment. The reactions considered are the oxygen reaction and the hydrogen reaction. These reactions are occurring simultaneously everywhere along the material/environment interface. Of course, local concentrations of dissolved species will favour one reaction or the other.
The hydrogen reaction (HR)

$$2H^+ + 2e^- \Leftrightarrow H_2 \tag{68}$$

has the electrode kinetics

$$i = 1.682\left[H_2\right]e^{\left(\frac{2F}{RT}0.099E\right)} - 7.89.10^{-4}\left[H^+\right]e^{\left(\frac{-2F}{RT}0.45E\right)} \tag{69}$$

where [H_2] is the dissolved hydrogen concentration [mol/m³], which is a global input parameter, but the actual local concentration is a calculated variable. [H^+] is the calculated proton concentration [mol/m³], E is the calculated electrode potential [V], F, R and T have their usual meaning and dimensions and i is the calculated current density [A/m²].
The oxygen reaction (OR)

$$O_2 + 4e^- + 2H_2O \Leftrightarrow 4OH^- \tag{70}$$

has the following electrode kinetics.

$$i = -0.18\left[O_2\right]^{0.66} e^{\left(\frac{4F}{RT}0.17E\right)} \tag{71}$$

[O_2] is the dissolved oxygen concentration [mol/m³] and is a general input parameter, but the local concentration is calculated. All other parameters have been defined previously.
The anodic corrosion reaction is, apart from the first term in eq. (69), the dissolution of the metal and is given by

$$M \Leftrightarrow M^{2+} + 2e^- \tag{72}$$

The electrode kinetics for this reaction at the crack tip are determined by expression (30) because the rate at which the metal dissolves, e.g. the current density at the crack tip, is assumed to be in accordance with the slip dissolution mechanism.

4.4 Calculation procedure

When the program is opened, the input matrix values (Table 4-2) can be entered in the user interface. The programme will then start the calculation. First, the grid of the fluid flow is generated and the flow field is calculated. Then the grid for the electrochemical calculations is generated and interpolated on the flow grid. This procedure has only to be carried out once, as the different electrochemical situations will not influence the flow field. Now, an initial value (2A/m²) for the average current density is imposed at the crack tip. Using this imposed current, the electrochemical calculations will result in a certain value for a new average current density through the slip dissolution formula (eq. 30). The obtained value for i_{avg}, is compared with the old value and updated. This iterative process keeps going on until the calculated value for i_{avg} satisfies the slip dissolution (SD) formula. The final step is the calculation of the crack propagation rate, using Faraday's law (eq. 27). The following flow chart shown in Figure 4-3 illustrates this calculation procedure.

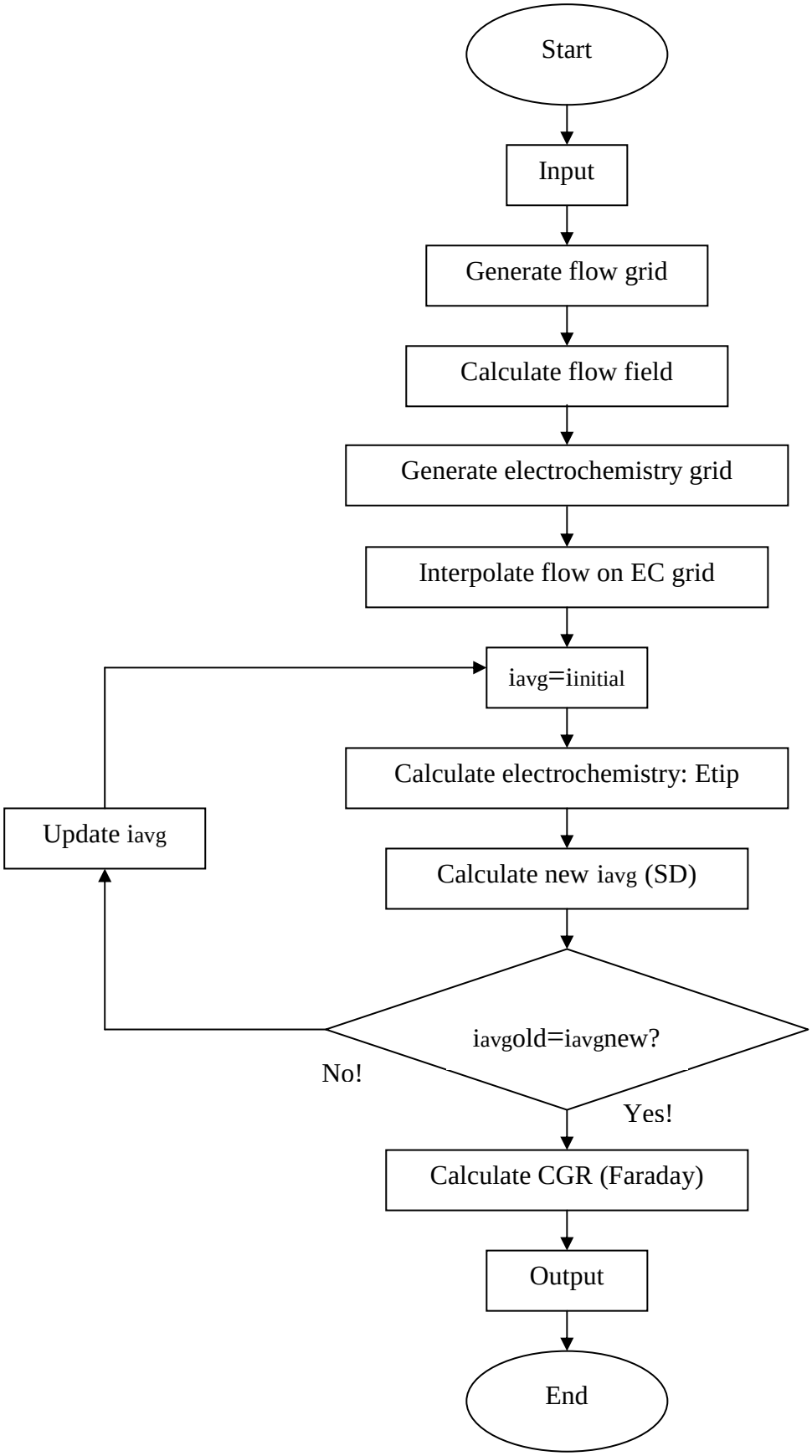

Figure 4-3: Flow chart of the calculation procedure of CGR-

5 Calibration of CGR-1 at reference temperature 320°C

5.1 Introduction

The CGR-1 software has first to be calibrated against a reference dataset at a certain temperature. Experimental data [14] are available to carry out this calibration procedure at a reference temperature of 320°C.
First, the calibration procedure will be introduced and the input matrix for the calibration will be discussed briefly to point out some uncertainties on parameters and assumptions. The actual calibration procedure will then be carried out and the results will be summarized in a few graphs and tables, followed by a discussion of the obtained results.
Effects due to irradiation are not included, but the variation of the mechanical properties with increasing neutron fluence or dpa[8] is quite similar to a variation in cold work. In general, an increase in dpa or and increase in amount of cold work will harden and strengthen the material.

5.2 Calibration procedure

The calibration procedure is carried out in a few successive steps. CGR-1 calculates the electrode potential at the crack tip for a number of crack tip currents, as explained in section 4.4. and is represented by the solid curve in Figure 5-1. This is the response of the environment to the applied current at the crack tip: the higher the current, the higher the potential drop from crack tip to crack mouth. This will give a first E_{tip}-I_{tip} relation. Expression (30) will provide a second relation (the dashed line in Figure 5-1) because all parameters, except E_{tip}, are constant for a given input matrix. For variable electrode potentials, different values for I_{tip} will be obtained.

$$i_{avg} = \left[\hat{i}_0 \exp\left(\frac{\alpha F}{RT} E_{tip} \right) \frac{1}{(1-m)} \left(\frac{t_0}{\varepsilon_f} \frac{M}{\rho z F} G \right)^m \right]^{\frac{1}{1-m}} \tag{30}$$

A final relation is given by Faraday's law: the experimental crack propagation rates in Table 5-1 will determine the current at the crack tip ($\dot{a} \square I_{tip}$). This reasoning is shown schematically in the Figure 5-1. The objective is now to determine a value for $\hat{i}_0$ for which the three curves all come together in the same point.

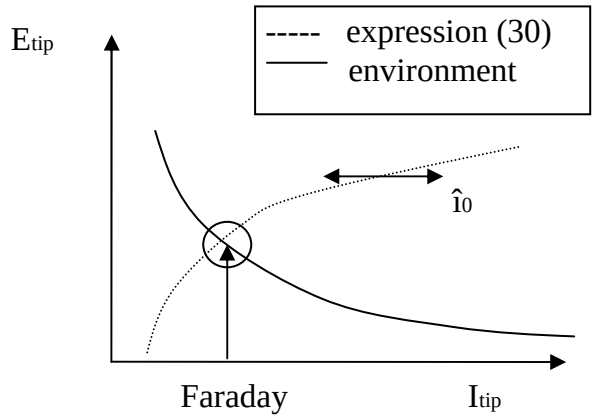

Figure 5-1: Schematic representation of the calibration procedure

[8] displacement per atom

The calibration is then carried out by 'shifting' the curve of expression (30) by changing $\hat{i}_0$ until it crosses the solid curve at the point where Faraday's law is valid.

5.3 The input matrix calibration set

The dataset that will be used for the calibration are variable in stress intensity for type 316 stainless steels that were given a certain amount of cold work [14]. Increasing the amount of cold work implies an increase in yield strength and a change in the work hardening exponent. The input matrix for the calibration at the reference temperature is shown in Table 5-1.

	K [MPa√m]	E [GPa]	v [-]	σy [MPa]	io [-]	m [-]	n [-]	L [mm]	B [ppm]	Li [ppm]	H_2 [cc/kg]	T [°C]	Re [-]	CPR_meas [m/s]	
5%CW	26	175	0,3	243	1	0,8	4,74	3,125	500	2	30	320	1000	6,00E-12	{1}
	35	175	0,3	243	1	0,8	4,74	3,125	500	2	30	320	1000	1,50E-11	{2}
	25,5	175	0,3	345	1	0,8	7,22	3,125	500	2	30	320	1000	3,20E-11	{3}
10%CW	26,5	175	0,3	345	1	0,8	7,22	3,125	500	2	30	320	1000	1,60E-11	{4}
	35	175	0,3	345	1	0,8	7,22	3,125	500	2	30	320	1000	3,60E-11	{5}
	14	175	0,3	495	1	0,8	6,9	3,125	500	2	30	320	1000	4,50E-12	{6}
	20	175	0,3	495	1	0,8	6,9	3,125	500	2	30	320	1000	4,40E-11	{7}
15%CW	24,5	175	0,3	495	1	0,8	6,9	3,125	500	2	30	320	1000	4,40E-11	{8}
	27	175	0,3	495	1	0,8	6,9	3,125	500	2	30	320	1000	6,50E-11	{9}
	37	175	0,3	495	1	0,8	6,9	3,125	500	2	30	320	1000	1,10E-10	{10}
	21,5	175	0,3	572	1	0,8	8,35	3,125	500	2	30	320	1000	6,40E-11	{11}
20%CW	25	175	0,3	572	1	0,8	8,35	3,125	500	2	30	320	1000	1,10E-10	{12}
	30	175	0,3	572	1	0,8	8,35	3,125	500	2	30	320	1000	1,10E-10	{13}
	42	175	0,3	572	1	0,8	8,35	3,125	500	2	30	320	1000	1,80E-10	{14}

Table 5-1: Input matrix for the calibration of CGR-1 at reference temperature

All factors from Table 5-1 are needed to carry out the calculations. Some of these parameters are taken from the article while for other factors, reasonable estimates or assumptions have to be made as explained hereunder.

- K, taken from [14]
- σ_y, taken from [14]
- B, taken from [14]
- Li, taken from [14]
- H_2, taken from [14]
- T, taken from [14]
- CPR_meas, taken from [14]

The number in accolades after CPR_meas, which is the experimentally measured crack propagation rate, is the case number.

- n, the work hardening exponent, is acquired after private communication with the author of the article.
- E, the Young's elasticity modulus is slightly temperature dependent which must be taken into account. Figure 5-2 shows this temperature dependency according to [15]. The same graph will be used for the calibration at varying temperatures (section 6).

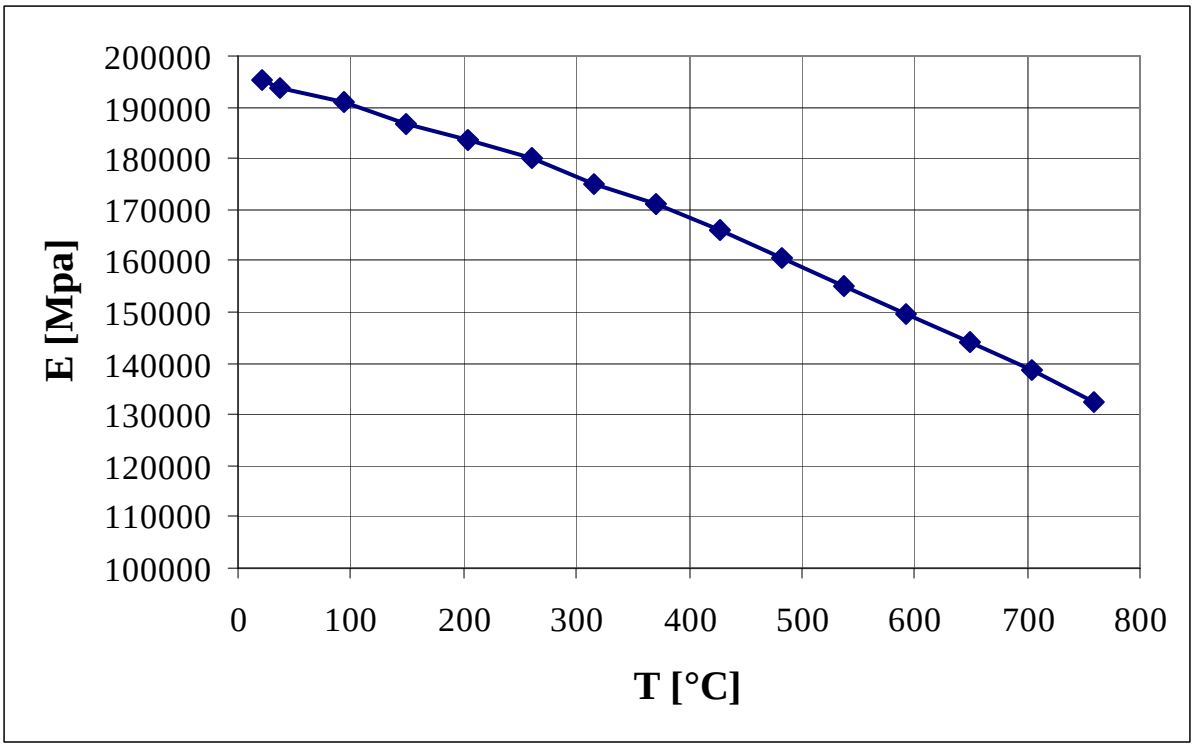

Figure 5-2: Temperature dependency of Young's elasticity modulus

- m, the repassivation parameter, is probably the most difficult parameter to assess, as it is dependent on the material and the environment. There is no literature data available concerning repassivation kinetics of type 316 stainless steels in PWR relevant conditions. Nevertheless, some experimental data [16-17] on this subject are available for other stainless steels and nickel alloys, for instance in, a slightly oxygenated diluted sulphuric acid environment[9]. These experimental data predict values for m that vary from about 0.5 to 1, with most values around 0.7 to 0.8. The final choice for m is a compromise in the few representative available data. After the final calibration, a sensitivity analysis of the effect of m on the CPR will be carried out.

The specimen used in the experiment is a 0.5CT[10] specimen which is shown in Figure 5-3.

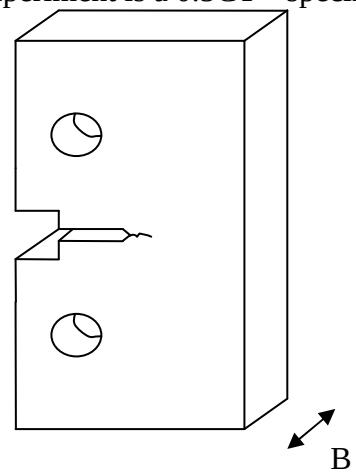

Figure 5-3: Schematic representation of a 0.5CT specimen

[9] This is a typical boiling water reactor (BWR) environment
[10] Compact Tension

- The specimen has a width of 25mm in the direction of the mechanical crack. There exists a difficulty in the determination of the actual crack length L because the mechanical and the electrochemical crack length are not the same. The electrochemical crack is located in the direction indicated by B in Figure 5-3, which is 12.5mm for a 0.5CT specimen. The real electrochemical crack will therefore have an undetermined length between 0 and 6.25mm, from the side of the specimen to the center. An intermediate value could therefore be at half of this maximum length, which is 3.125mm in this case. Like in the situation of the repassivation parameter, the sensitivity of the crack propagation rate with varying crack lengths will be investigated after CGR-1 has been calibrated.
- Re, the Reynolds number, which will fix the inlet flow conditions in the main channel, has been set at a value of 1000 as in the CGR-1 reference case, since no information on flow conditions is provided in [14].
- The oxygen concentration can be adjusted, but will set equal to zero. This is a reasonable assumption because hydrogen is introduced on purpose to avoid the presence of molecular oxygen in the system, which will enhance corrosion rates.

5.4 Calibration against reference dataset

The $\hat{i}_0$ from expression (30) is the real maximum current density that is emanating from the crack tip, immediately after film rupture. This parameter is shown graphically in Figure 3-2 and is not directly accessible from the user interface. Nevertheless, this factor can be altered in a parameter list that also contains all constants from Table 4-1. CGR-1 uses this list to calculate internally the crack propagation rate with the use of expression (30). None of the parameters in this list plays a role in the computation of the environments response to an imposed crack tip current. This $\hat{i}_0$ is indirectly accessible from the user interface by i_0, the sensitization factor from Table 5-1. The actual value that CGR-1 uses for the calculation of the crack propagation rate is then obtained from the multiplication of the sensitization factor and the real maximum current density: $\hat{i}_0.i_0$.
At this stage, nothing is known about the result that will be calculated, so i_0 is set equal to 1 and CGR-1 will calculate with the real $\hat{i}_0$ from the parameter list. As received from the CGR-1 software developer, the initial value for $\hat{i}_0$ in the list of parameters appears to be $4.9\ 10^6$.
For the first step of the calibration, i_0 will be kept constant at a value of 1 and a new value $\hat{i}_0$ will be calculated. As equation (30) is an analytical expression and E_{tip} is computed independently from equation (30), $\hat{i}_0$ can easily be calculated with a regular worksheet for all cases in Table 5-1 with the procedure described in 5.2
When all values for $\hat{i}_0$ are updated for all 14 cases, two approaches will be followed to make a fitting of all calculated current densities. After these fitting procedures, $\hat{i}_0$ will be given a new constant value in the parameter list and i_0, in the input interface, will then be calculated with respect to this new $\hat{i}_0$.

The first calculation is carried out against one single experimental reference point. This point is arbitrarily chosen to be case 2 in Table 5-1. The calibration is carried out as described previously and the obtained calibration factor $\hat{i}_0$ is identified as $6.06\ 10^6$ A/m².
At this moment, it is assumed that there is only one numerical value for $\hat{i}_0$.
This value is stored in the list of parameters in CGR-1 and all other cases are calculated with this newly obtained calibration factor. The results of these calculations are graphically shown in Figure 5-4.
In this graph, the results of the calculated crack propagation rates are plotted against the experimental values on a one-to-one scale.

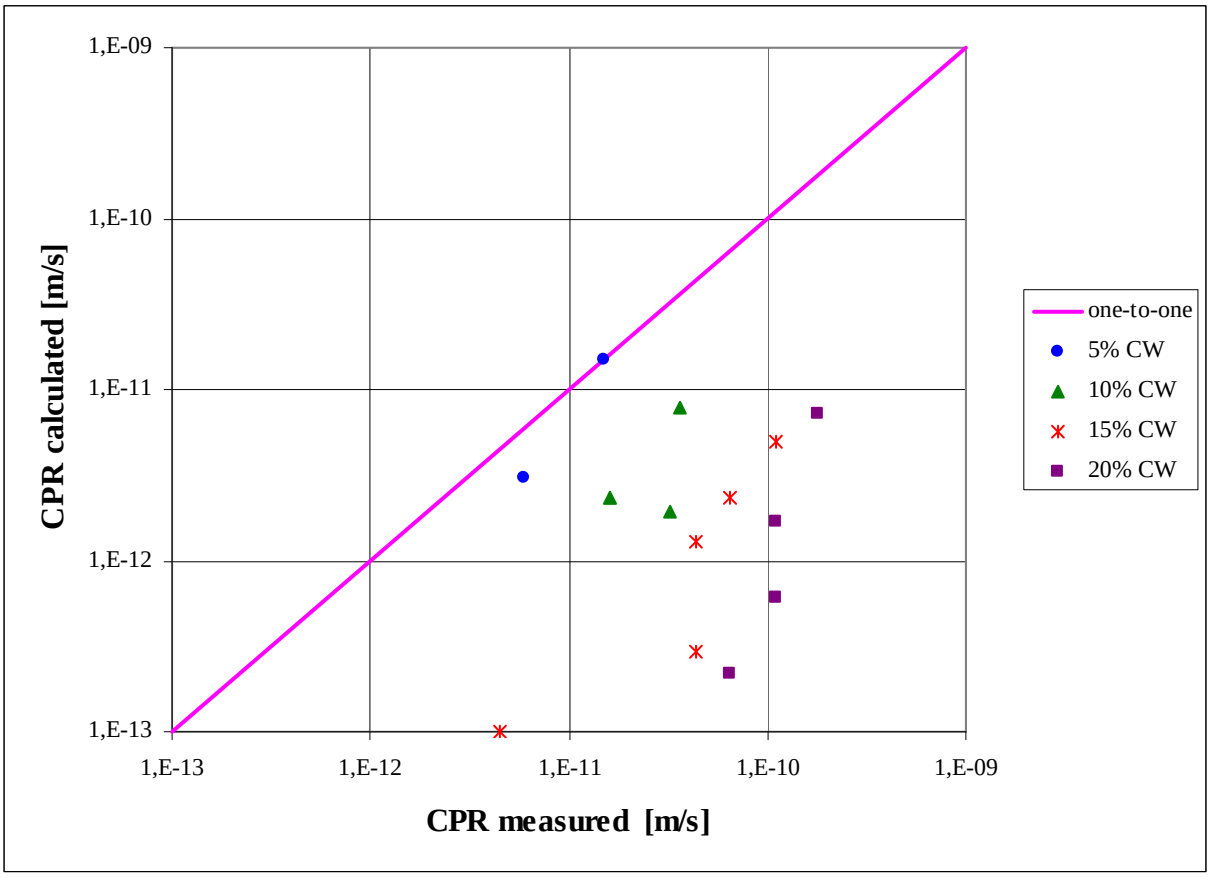

Figure 5-4: One to one plot of calculated and experimental crack propagation rate with calibration at reference point (case 2)

The agreement is very poor, but some useful observations can be made. The calculated trend 'follows' quantitatively and very roughly the experimental one, although the actual difference in CPR is up to three orders of magnitude. A second observation is that the disagreement is enhanced when the amount of cold work given to the material increases.
This observation clearly suggests that one single value for $\hat{i}_0$ is not satisfactory. As the result for the computation of the environment is independent of $\hat{i}_0$, $\hat{i}_0$ can be calculated for all cases as described in the calibration procedure. The results of all these calculations are summarized in Table 5-2.
According to [18], $\hat{i}_0$ is a function of yield strength and is expressed as follows:

$$\hat{i}_0 = \hat{i}_0^0 \exp\left(\frac{V_m \sigma_y}{RT}\right) \tag{73}$$

where V_m is the molar volume [m³/mol] and $\hat{i}^0_0$ is a pre-exponential parameter [A/m²]. The molar volume is defined as the ratio of the molar mass M and the density ρ[11] and is equal to 7.10522 10^{-6} m³/mol. The other factors have their usual meaning and dimensions.
Two approaches are used for the fitting of the calibrated points. First, the calculated data for $\hat{i}_0$ are fitted with an exponential trend curve on an $\hat{i}_0$-σ_y graph:

$$\hat{i}_0 = \hat{i}_0^0 \exp\left(A\sigma_y\right) \tag{74}$$

Here, A is just a value [1/MPa] that is given by the fitting. Then, new values for $\hat{i}_0$ will be obtained by using expression (73) and optimising for $\hat{i}^0_0$. This is done by imposing an initial

[11] Numerical values for M and ρ can be found in Table 4-1

value for $\hat{\imath}^0_0$, calculating $\hat{\imath}_0$ with expression (73) and minimizing the sum of squares of the difference of these new values for $\hat{\imath}_0$ and the original values for $\hat{\imath}_0$. The results of this individual calibration and the calculations are presented in the following graph and tables.

	Case	$\hat{\imath}_0$ (data) [A/m²] (eq.74)	σ_y [MPa]	$\hat{\imath}_0$ (V_m) [A/m²] (eq.73)
5%CW	1	6069000	243	8653042
	2	6058000	243	8653042
10%CW	3	10580000	345	10023198
	4	8818500	345	10023198
	5	8772500	345	10023198
15%CW	6	17615000	495	12441849
	7	14877000	495	12441849
	8	11770000	495	12441849
	9	11783000	495	12441849
	10	10493000	495	12441849
20%CW	11	16155000	572	13901958
	12	15416000	572	13901958
	13	12910000	572	13901958
	14	11845000	572	13901958

Table 5-2: Individual alibration factors at reference temperature 320°C

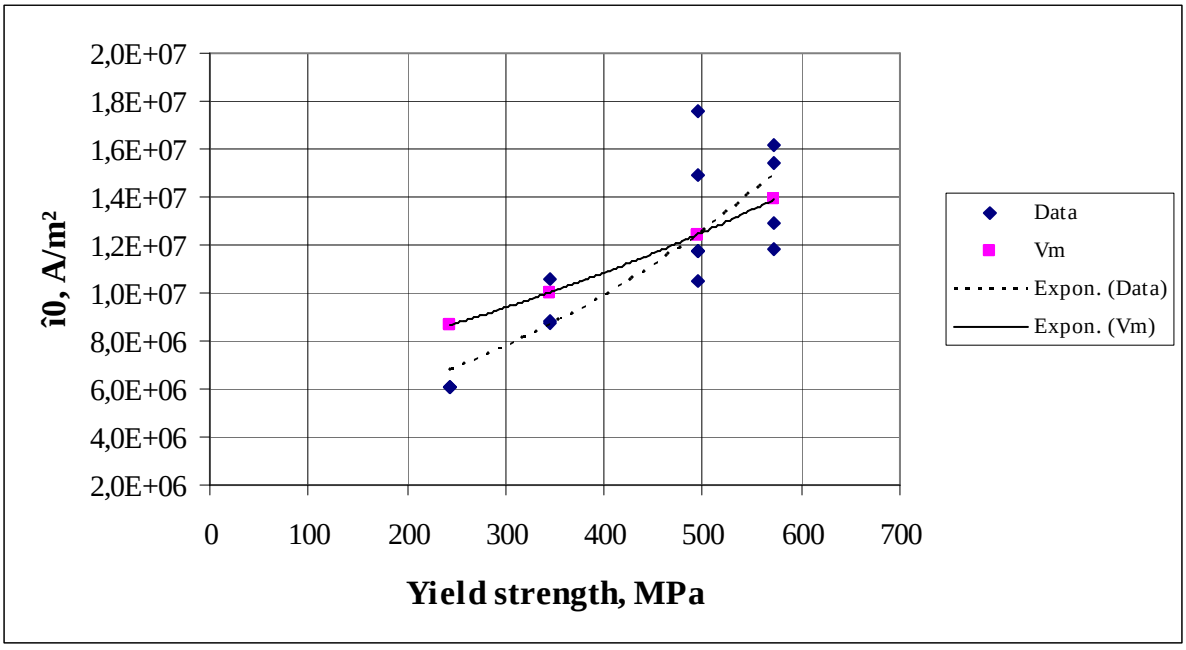

Figure 5-5: Fitting of calculated data and theoretical approach Vm

Parameter	Best fitting of the calculated data (eq. 74)	Theoretical molar volume V_m (eq. 73)
R [J/molK]	8,31441	8,31441
T[K]	593,15	593,15
A [1/Mpa]	2,40541E-03	-
Vm [m³/mol]	**1,18627E-05**	**7,10522E-06**
$\hat{\imath}^0_0$ A/m²	**3,77442E+06**	**6,09657E+06**

Table 5-3: Results of calibration at reference temperature

The molar volume in Table 5-3 for the best fitting of the calculated data is obtained by assuming that A is defined as V_m/RT as suggested by equations (73) and (74). There is a slight difference in molar volume V_m and pre-exponential $\hat{\imath}^0_0$ between both approaches as expected from Figure 5-5. The calibration factor $\hat{\imath}_0$ in the parameter list will now be fixed to 1.10^7; an arbitrary intermediate value (see Figure 5-5) as explained before. The sensitization parameter i_0 in the input programme can now easily be adjusted to every independent case by taking the ratio of the fitted data points and the new $\hat{\imath}_0$ value in the list of parameters.
Table 5-4 shows the result of these computations for the best fitting of the calculated data and for the theoretical approach. All 14 cases are now calculated again after the calibration with the adapted sensitization parameter.

Best fitting of the calculated data (eq. 74)			**Theoretical molar volume V_m (eq. 73)**		
Case	i_0-factor	CGR_calc [m/s]	i_0-factor	CGR_calc [m/s]	CPR_meas [m/s]
1	0,68	1,07E-11	0,87	3,17E-11	**6,00E-12**
2	0,68	2,50E-11	0,87	6,47E-11	**1,50E-11**
3	0,87	1,33E-11	1,00	2,51E-11	**3,20E-11**
4	0,87	1,51E-11	1,00	2,86E-11	**1,60E-11**
5	0,87	3,50E-11	1,00	6,03E-11	**3,60E-11**
6	1,24	7,92E-13	1,24	7,92E-13	**4,5E-12**
7	1,24	1,91E-11	1,24	1,91E-11	**4,40E-11**
8	1,24	5,60E-11	1,24	5,60E-11	**4,40E-11**
9	1,24	8,25E-11	1,24	8,25E-11	**6,50E-11**
10	1,24	1,85E-10	1,24	1,85E-10	**1,10E-10**
11	1,49	4,49E-11	1,39	3,30E-11	**6,40E-11**
12	1,49	9,61E-11	1,39	7,35E-11	**1,10E-10**
13	1,49	1,79E-10	1,39	1,44E-10	**1,10E-10**
14	1,49	3,42E-10	1,39	2,90E-10	**1,80E-10**

Table 5-4: Calculated crack propagation rates after the calibration at 320°C

Finally, a new one-to-one plot of the measured CPR and the calculated CPR can be constructed and a comparison between the two approaches, as discussed above, can be made.

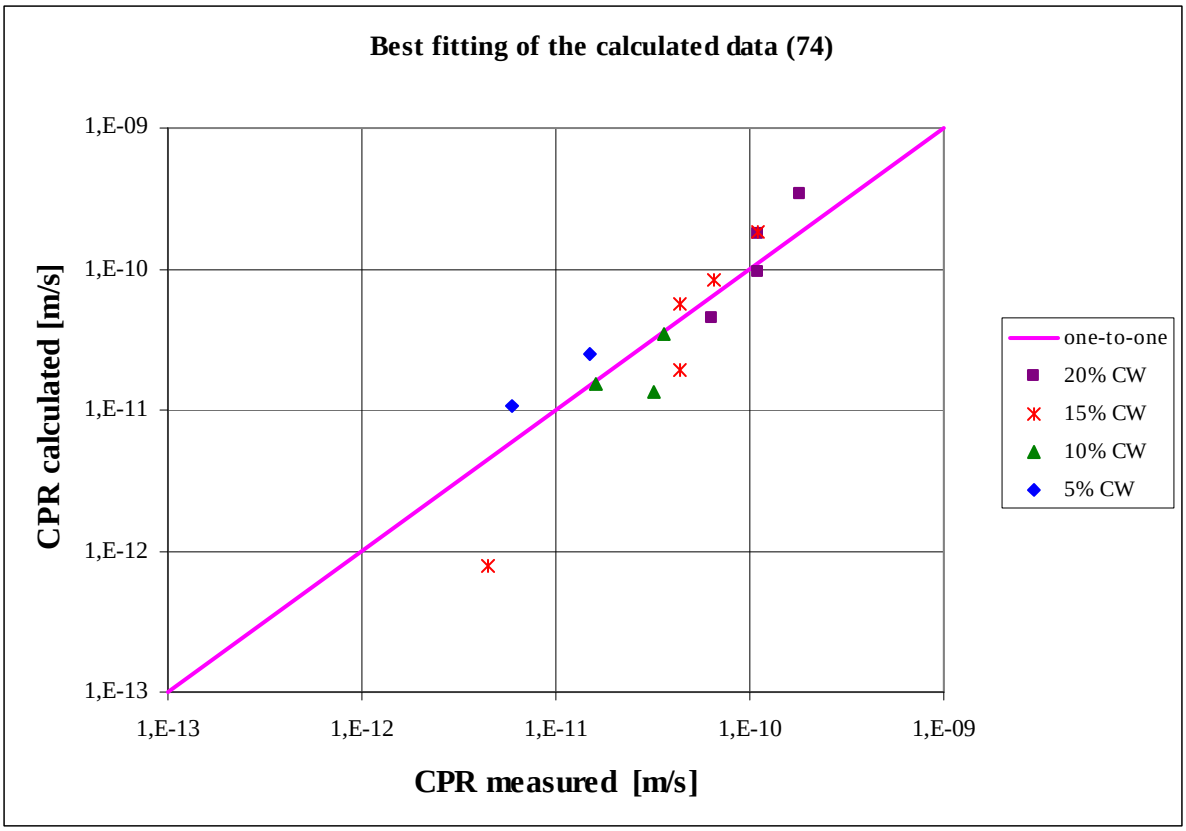

Figure 5-6: One-to-one plot of calculated and measured crack propagation rate after calibration with best fitting of the calculated data

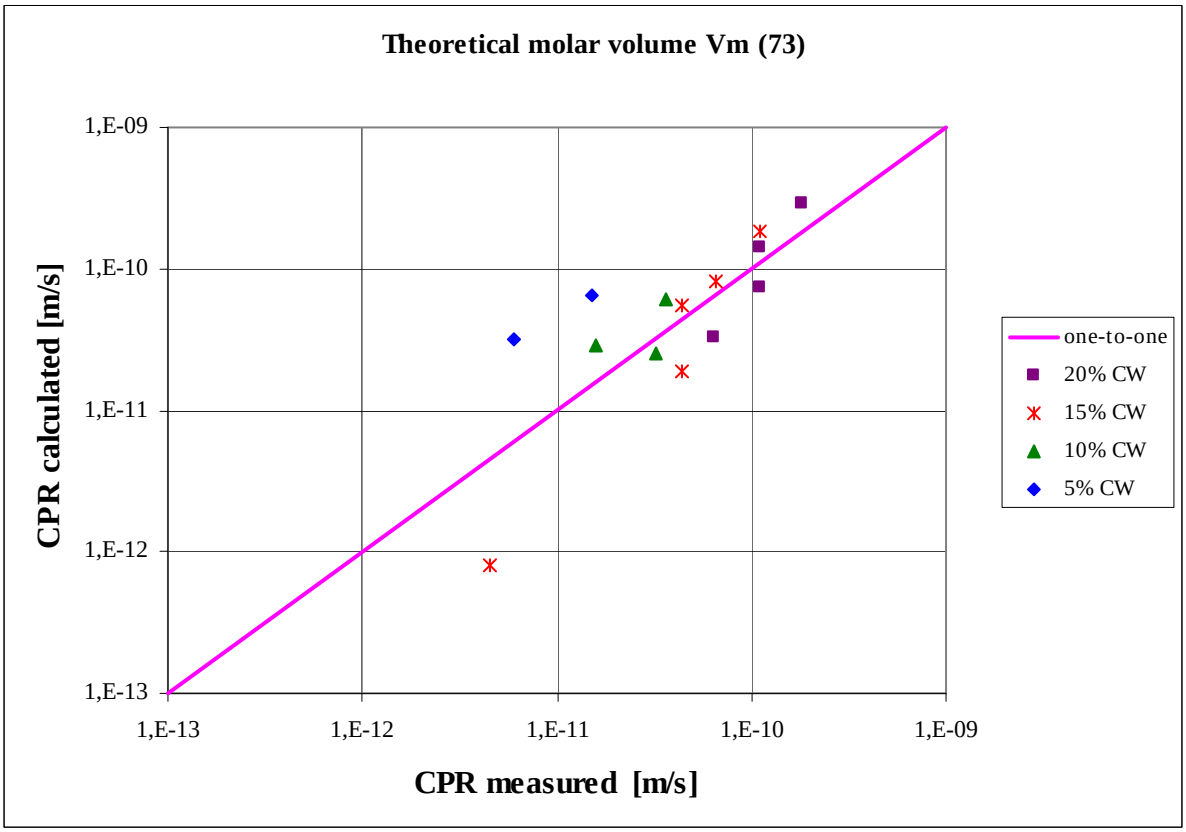

Figure 5-7: One-to-one plot of calculated and measured crack propagation rate after calibration with theoretical molar volume Vm

Comparing the results after the calibration with the initial one (Figure 5-4), it is obvious that major improvement has been made in the acquired results. The results for the two calibration approaches are only slightly different, especially at higher yield strengths.

5.5 Discussion and conclusions

CGR-1 has now been calibrated at the reference temperature of 320°C. Two approaches have been suggested during the calibration procedure, one with a best fitting for the calibrated data with two varying parameters and another with a more theoretical approach.
There is an obvious dependency of the maximum bare metal current density (i_0) on the yield strength (or % CW) of the material.
A possible explanation is as follows. Increasing the amount of cold work will increase the amount of dislocations significantly, which is translated into microscopical stresses and strains. These stresses and strains will increase the energy in the metallic lattice.
Thermodynamically, the system is brought in a higher energy state through an increase in Gibbs free energy. If the passivating film is suddenly ruptured, the bare metal at the surface with a higher free energy will cause enhanced dissolution. Hence, the bare metal current density (i_0) at the moment of film rupture will be higher.
The final result for the calibration at reference temperature is quite satisfying, although some additional remarks can be made.
A particularity can be noticed if the experimental results for the CPR of cases 3 and 4 are compared. Here, the crack propagation rate goes down with a factor of 2, while the stress intensity increases slightly from 25.5 to 26.5MPa$\sqrt{m}$. Experimental error and variability of the measured crack propagation rates has to be taken into account.
Nevertheless, taking into account all approximations, assumptions and possible errors, the calibration of CGR-1 is satisfactory.
The next step will be, starting from these obtained results, to calibrate CGR-1 for varying temperatures. This procedure will be carried out with both approaches as explained above.

6 Temperature calibration of CGR-1

6.1 Introduction

The CGR-1 software is now calibrated at a reference temperature 320°C for the effect of cold work. The next step in the calibration procedure is the calibration of CGR-1 if the temperature is the only variable. From previous chapters, it is obvious that temperature plays a very significant role in the phenomenon of stress corrosion cracking. It is not only a parameter in the slip dissolution formula, but the temperature also influences the environmental conditions. Water density, diffusion coefficients, (electro)chemical reaction rates… are all function of temperature. It becomes even more complicated because some input parameters are also temperature dependent. The temperature dependence of Young's modulus, for instance, has been evaluated earlier in Figure 5-2.
The procedure for this calibration is completely analogous as in section 5.2.
The first part of this chapter will therefore consist of an evaluation of the temperature dependence of the yield strength. The actual calibration procedure will then be carried out according to an experimental dataset from [14] and, finally, some conclusions concerning this procedure will be drawn.

6.2 The input matrix calibration set

The dataset [14], which is used to carry out the calibration procedure, is shown in Table 6-1.

	K [MPa√m]	E [GPa]	ν [-]	σy [MPa]	io [-]	m [-]	n [-]	L [mm]	B [ppm]	Li [ppm]	H_2 [cc/kg]	T [°C]	Re [-]	CPR_meas [m/s]
	30	179	0,3	577	1,39	0,8	8,35	3,125	500	2	30	270	1000	1,50E-11 {15}
20%CW	30	177	0,3	575	1,39	0,8	8,35	3,125	500	2	30	290	1000	2,80E-11 {16}
	30	175	0,3	572	1,39	0,8	8,35	3,125	500	2	30	320	1000	1,20E-11 {17}

Table 6-1: Input matrix for the calibration of CGR-1 at varying temperatures

Some parameters in Table 5-1 are taken from the article while for others, reasonable estimates or assumptions have to be made.

- K, taken from [14]
- B, taken from [14]
- Li, taken from [14]
- H_2, taken from [14]
- T, taken from [14]
- CPR_meas, taken from [14]
- n, see section 5.3 and below
- m, see section 5.3
- L, see section 5.3
- Re, see section 5.3
- E, see section 5.3 and Figure 5-2
- i_0, see section 5.4
- σ_y, see below

It is assumed that, apart from the Young's modulus, only the yield strength σ_y is temperature dependent although it can be expected that also the repassivation parameter m is not independent of temperature. The uncertainty on a realistic estimation of m, even at one single temperature, is quite significant due to the unavailability of good experimental data.

This parameter will therefore be kept constant. If more information on this important unknown is gathered, the same procedure can be followed to recalibrate the programme.
In general, temperature dependencies of material properties change according to an Arrhenius like behaviour. This behaviour is usually expressed with an exponential function as follows:

$$x = x_0 \exp\left(\frac{-E_a}{RT}\right) \tag{75}$$

Where x is the temperature dependent property, x_0 is a pre-exponential and E_a is the characteristic activation energy [kJ/mol]. R and T have their usual meaning and dimensions. When this type of expressions is plotted on a log(x)-1/T graph, the typical straight Arrhenius curve is obtained. The activation energy can then easily be deduced from the slope of the curve.
The activation energy of the work hardening exponent n does not change a lot with temperature. According to [19], the activation energies of n are much less than 1kJ/mol.K, which is negligible in the relevant temperature range. Nevertheless, very few data concerning the temperature dependence of n are available.
It is assumed that all other parameters, thus except from yield strength and elasticity modulus do not change with temperature.

Data from [14, 19, 20] is used to investigate the temperature dependence of yield strength for different percentages of cold work at PWR relevant temperatures. These data are summarized in Table 6-2. Applying expression (75) on the mechanical property yield strength, the following is obtained.

$$\sigma_y = \sigma_{y0} \exp\left(\frac{-E_a}{RT}\right) \tag{76}$$

Temperature	**Sol. Annealed [19]**	**5% CW [14]**	**10% CW [14]**	**15% CW [14]**	**20% CW**	**SA[12]+WR[13] [20]**	**SA+CR[14] [20]**
23°C (RoomT)	336 362	358	499	596	[14] 625 [19] 709	568 775	1035
287°C	237 243						
300°C	308					499 608	827
320°C	271	243	345	495	[14] 572 [19] 567		
340°C	251						
Pre-exponential	193,26	164,26	237,59	410,3	[14] 523 [19] 460	433,63 467,34	648,44
Activation Energy[kJ/mol]	**1,45**	**1,93**	**1,84**	**0,93**	[14] **0,44** [19] **1,06**	**0,67** **1,25**	**1,16**

Table 6-2: Temperature dependence of yield strength [MPa]

The data from [14] will be used to perform the calibration, so a graphical representation of the typical Arrhenius curves is also provided in Figure 5-1.

[12] Solution Annealed
[13] Warm Rolled
[14] Cold Rolled

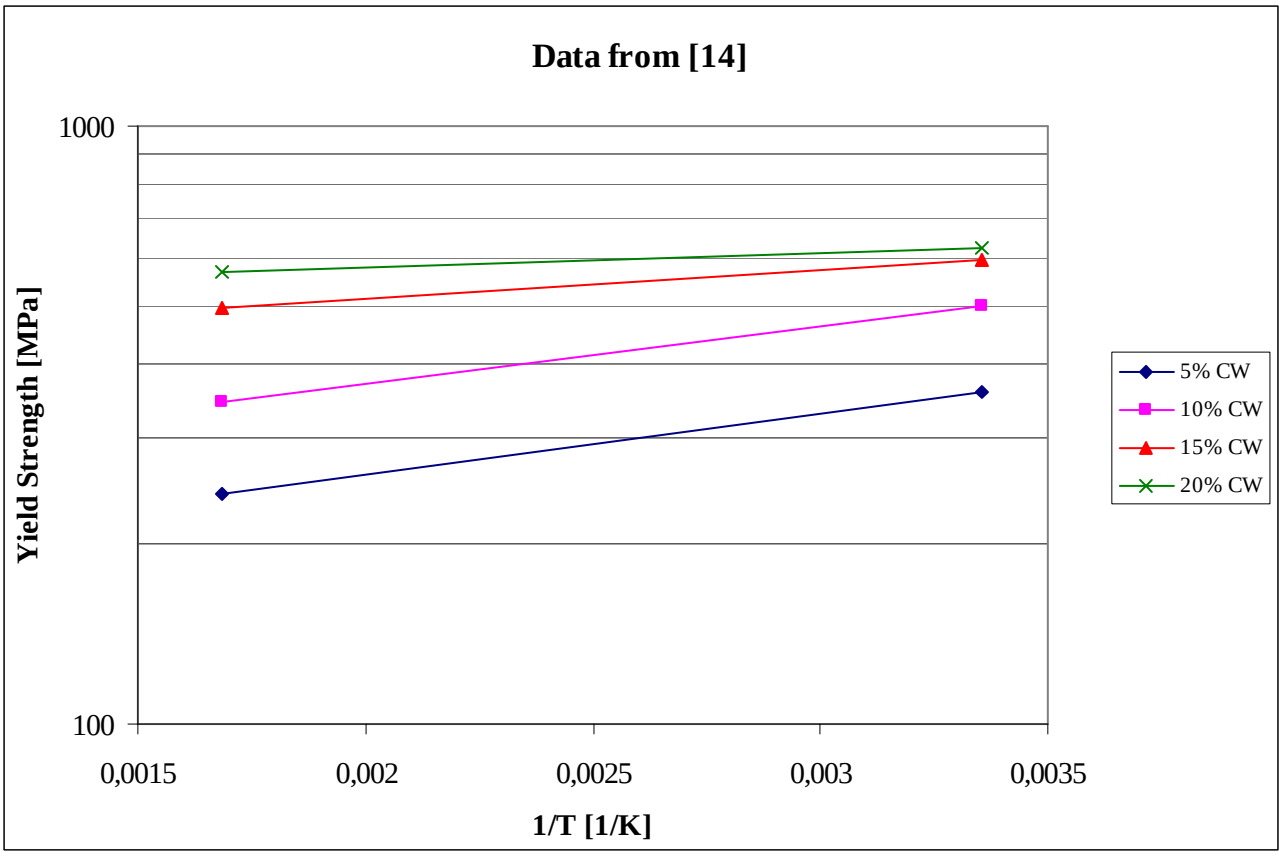

Figure 6-1: Temperature dependence of yield strength

It is obvious that the yield strength changes with varying temperatures, although the activation energies are relatively low. The energies never exceed 2kJ/mol, which can be translated to about 0.2 to 0.4MPa/K.

6.3 The calibration

The temperature dependencies of the elasticity modulus and the yield strength have been taken into account. The temperature varies from 270 to 320°C, which is a very normal temperature range for PWR's. The calibration procedure is exactly the same as explained in section 5.2: the cases will be calculated with the already obtained sensitization parameter. This can be easily done because case 17 is exactly the same as case 13 in the calibration at reference temperature. The sole difference between the two procedures is that, as thermally activated processes are investigated, a value for the activation energy has to be obtained.

To start with, case 15 and 16 are calculated with the sensitization factor of case 17 and the new $\hat{\imath}_0$ is obtained with the procedure already explained. As aforementioned, two approaches will be used: the results for a best fitting of the data and the more theoretical approach with the real molar volume. The result of the calibration is shown on an $\hat{\imath}_0$-1/T plot in Figure 5-2.

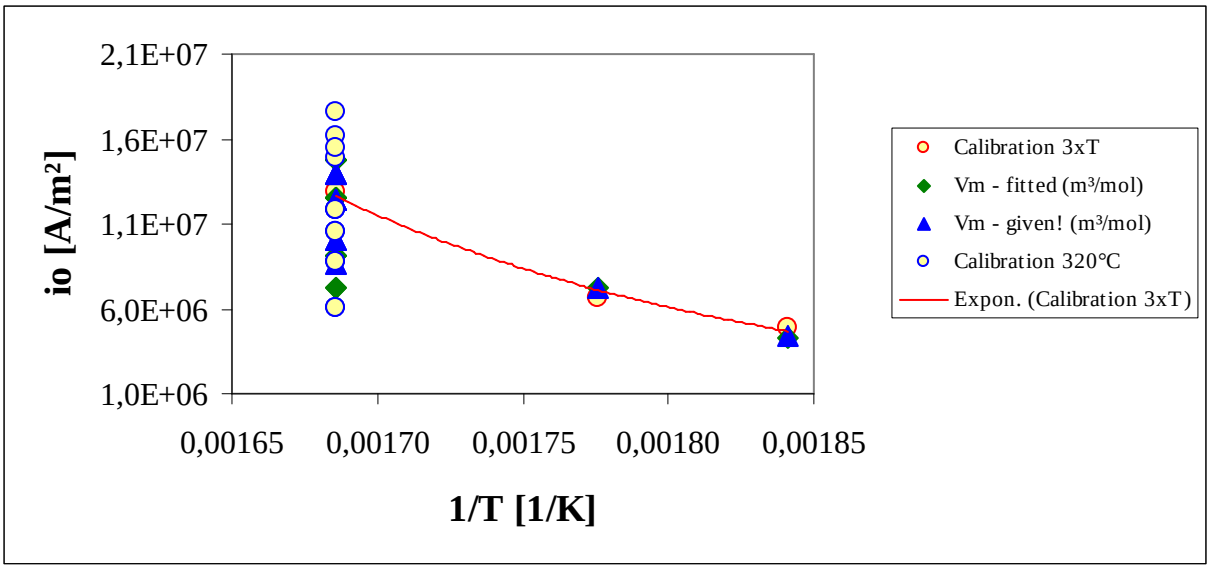

Figure 6-2: Graphical results for the calibration at varying temperatures and at 320°C

The indication 3xT means that the calibration has been carried out only for the data in Table 6-1. Vm-fitted and Vm-given are the fitted and theoretical approach of all calibrated data. The obtained results are expected to be expressible as equation (77).

$$\hat{i}_0 = \hat{i}_0^0 \exp\left(\frac{-E_a + \sigma_y V_m}{RT}\right) \tag{77}$$

The best fitting procedure is here fitted with three variable parameters (E_a, V_m, $\hat{i}^0_0$). The more theoretical approach is similar, except for the molar volume of course. The results of this procedure are summarized in succeeding tables and graphs.

Parameter	Best fitting of the calculated data	Theoretical molar volume V_m
Ea [J/mol]	70589	60467
Vm [m³/mol]	1,17E-05	7,11E-06
$\hat{i}^0_0$ A/m²	6,27E+12	1,23E+12

Table 6-3: Results for the calibration at temperature, see equation (80)

Best fitting of the calculated data			Theoretical molar volume V_m		
Case	i0-factor	CGR_calc [m/s]	i0-factor	CGR_calc [m/s]	CPR_meas [m/s]
1	0,68	1,07E-11	0,82	2,47E-11	**6,00E-12**
2	0,68	2,50E-11	0,82	5,23E-11	**1,50E-11**
3	0,87	1,36E-11	0,95	1,99E-11	**3,20E-11**
4	0,87	1,51E-11	0,95	2,28E-11	**1,60E-11**
5	0,87	3,50E-11	0,95	4,93E-11	**3,60E-11**
6	1,24	7,36E-13	1,18	6,26E-13	**4,50E-12**
7	1,24	1,88E-11	1,18	1,51E-11	**4,40E-11**
8	1,24	5,60E-11	1,18	4,49E-11	**4,40E-11**
9	1,24	8,10E-11	1,18	6,77E-11	**6,50E-11**
10	1,24	1,99E-10	1,18	1,61E-10	**1,10E-10**
11	1,48	4,42E-11	1,32	2,65E-11	**6,40E-11**
12	1,48	9,35E-11	1,32	5,71E-11	**1,10E-10**
13	1,48	1,74E-10	1,32	1,19E-10	**1,10E-10**
14	1,48	3,41E-10	1,32	2,46E-10	**1,80E-10**
15	0,46	1,18E-11	0,47	1,33E-11	**1,50E-11**
16	0,75	4,71E-11	0,72	3,90E-11	**2,80E-11**
17	1,48	1,74E-10	1,32	1,19E-10	**1,20E-10**

Table 6-4: Newly obtained crack calculated crack propagation rates and corresponding sensitization factors

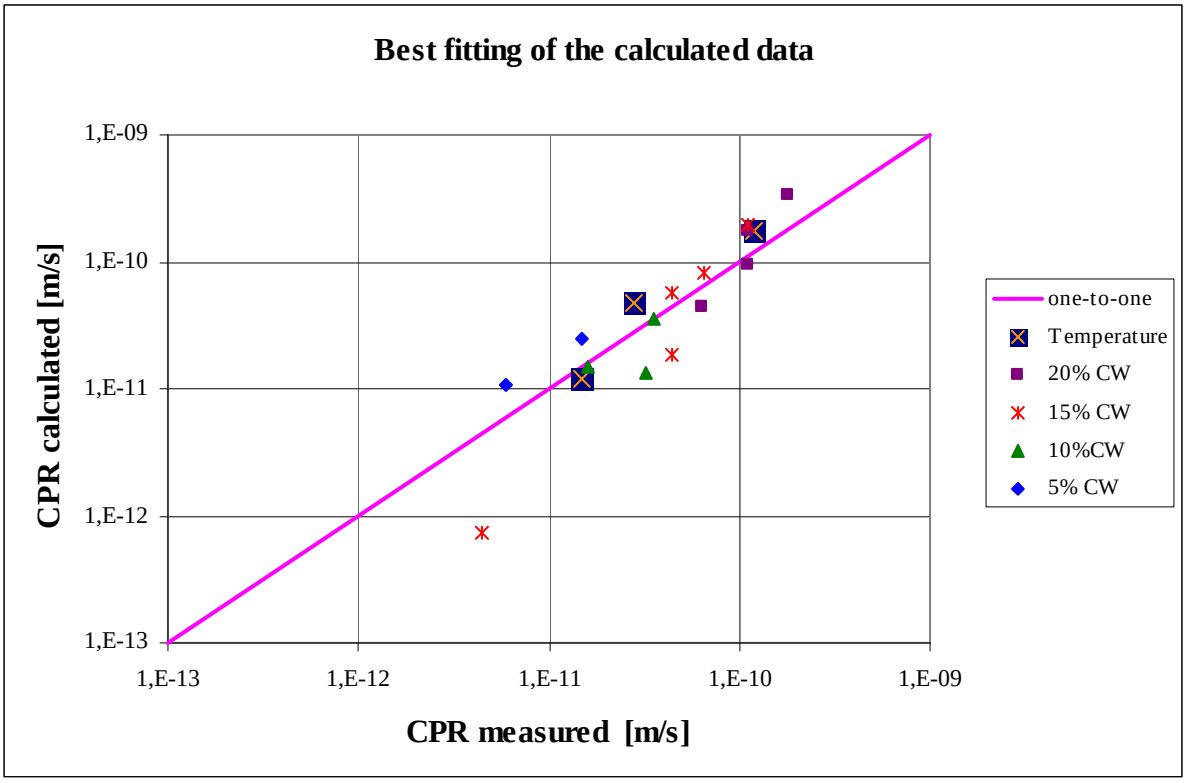

Figure 6-3: One-to-one plot of the measured and calculated crack propagation rates with best fitting of the calculated data

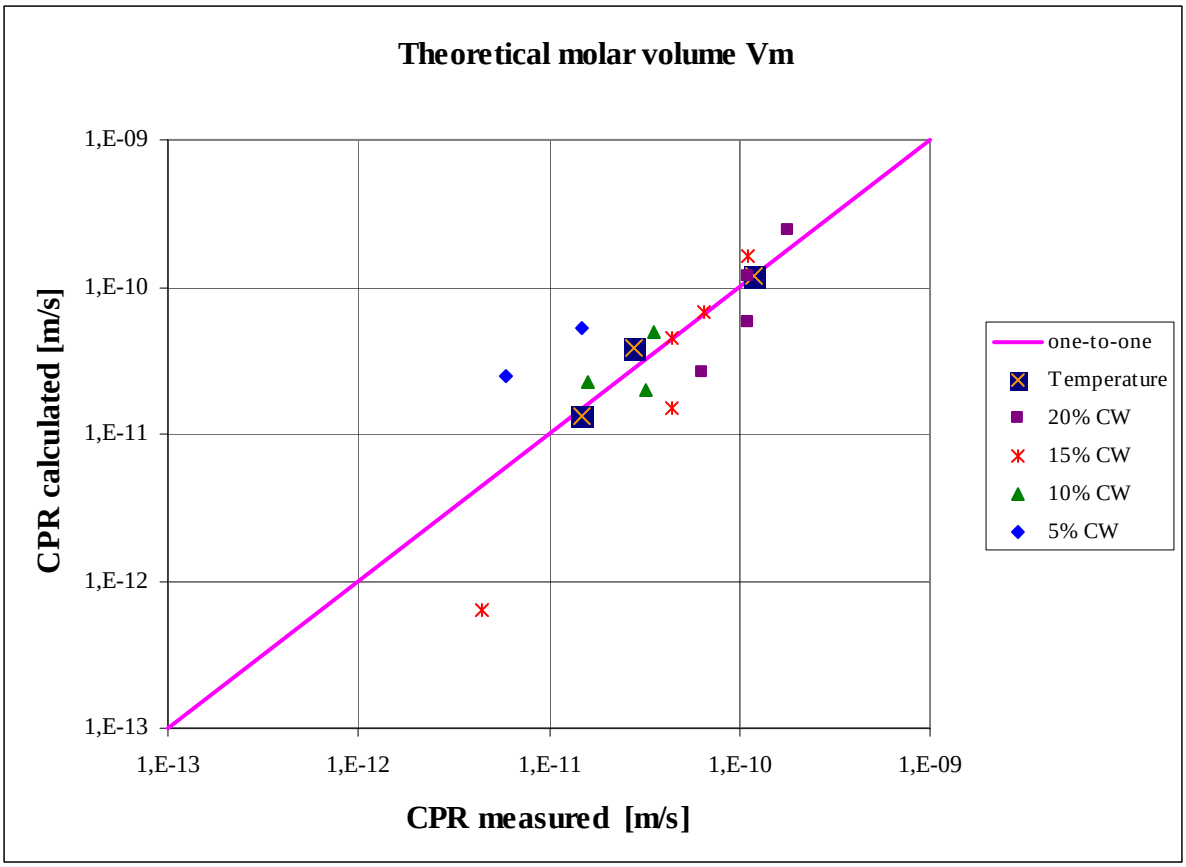

Figure 6-4: One-to-one plot of the measured and calculated crack propagation rates with the theoretical molar volume

6.4 Discussion and conclusions

The conclusions of this calibration procedure are essentially the same as for the calibration at the reference temperature of 320°C. The results for the best fitting of the data are slightly better than for the more theoretical approach, as expected. At higher yield strengths, however, the difference is negligible. The difference between both approaches at lower yield strengths (lower %CW) is quite significant.

Some other interesting issues can be discussed from these newly obtained results. First, the activation energy of the measured and calculated crack propagation rates can be acquired from the results. Figure 6-5 is a graphical representation of this reasoning.

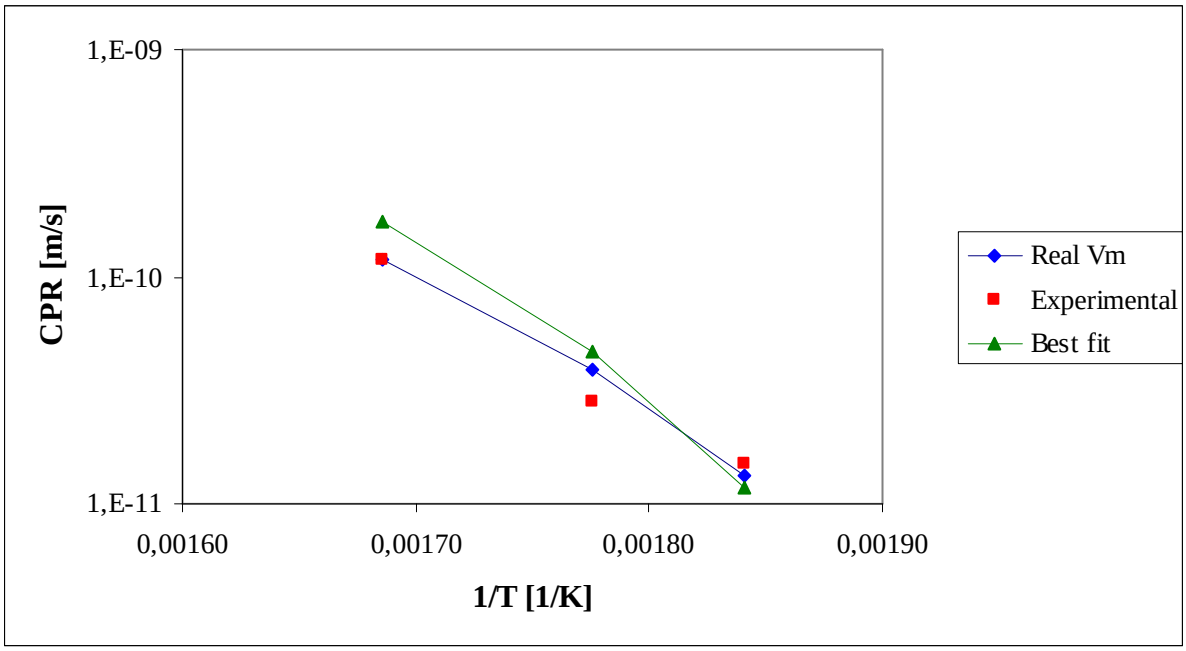

Figure 6-5: Temperature dependence of measured and calculated crack propagation rates

For the determination of the activation energy, expression (78) is used.

$$CPR = CPR_0 \exp\left(-\frac{E_a}{RT}\right) \tag{78}$$

The activation energy for the calculated CPR's is 142.8kJ/mol for the best fitting of the data and 116.5kJ/mol for the more theoretical approach with the real molar volume. The activation energy for the measured data is only 112.8kJ/mol, while the author of the article mentions an activation energy of about 100kJ/mol. Although the results of the best fitting are slightly better, the predicted activation energy for equation (78) is much better approached if the theoretical molar volume is used for the calibration.
Another interesting conclusion deals with equation (77). In this equation, the factor $Vm.\sigma_y$ is added to the activation energy. This factor is about 5-10% of the activation energy, depending on the yield strength. If the yield strength increases, the exponential term becomes smaller and the slope of the curve on an Arrhenius plot becomes less steep with increasing amount of cold work. This would imply that increasing amounts of cold work given to a material makes its crack propagation rate less dependent of temperature. This observation is experimentally verified by [21].

7 Effect of stress intensity

7.1 Introduction

The actual purpose of a programme like CGR-1 is to be able to perform trend calculations, for instance, to calculate how the crack propagation rate will change if some environmental or mechanical property differs from the reference case. This is essentially how CGR-1 has been calibrated: changes in yield strength, work hardening exponent, stress intensity and temperature have been used to approximate the measured crack propagation rate.
One of the most important relations that can be found in the literature is one between the crack propagation rate and stress intensity. The results and discussion of this relation will be discussed hereunder. Moreover, the trend calculation of CPR with respect to stress intensity is treated separately because the dataset from [22], used for the calibration, are represented in a CPR-K relation. This means that at least one important trend can be calculated and compared to literature data.

7.2 Trend calculation

7.2.1 Relation CPR-K

Figure 7-1 and Figure 7-2 show the result of the calculations as already done in previous chapters when dealing with the calibration of CGR-1.

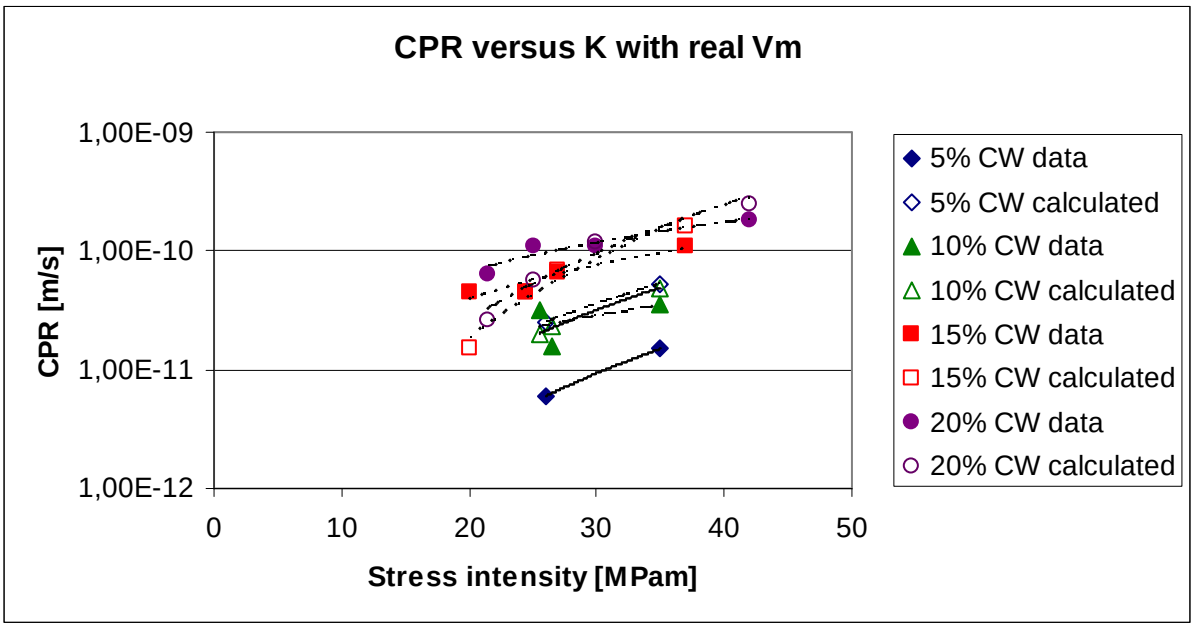

Figure 7-1: Stress intensity versus crack propagation rate with theoretical molar volume

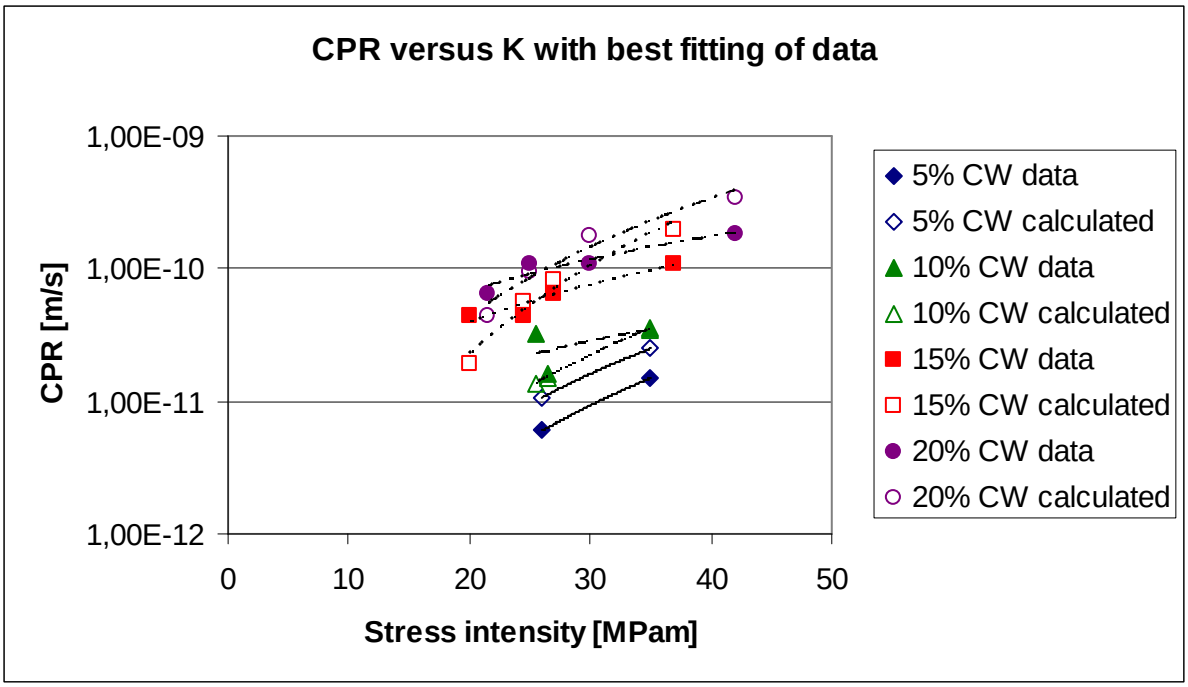

Figure 7-2: Stress intensity versus crack propagation rate with best fitting of the data

The measured data are quite well approximated by the calculated results, but an unsatisfying situation is observed for low yield strengths. In Figure 7-1 and less pronounced in Figure 7-2, the predicted crack propagation rates for the materials that were 5% cold worked are much higher than the experimental ones. They are more or less situated in the 10% CW range, which is unreasonably high. Although this problem might seem quite difficult to solve, there is a reason why this illogical trend is observed.

7.3 Plane stress versus plane strain

In chapter 3.3.2 and 3.3.3, two different expressions for the crack tip strain rate have been mathematically derived, one for plane strain and one for plane stress. Up till now, only the formula for the plane stress crack tip strain rate has been used. This is mainly due to the fact that this is the only model programmed in the software of CGR-1. Nevertheless, as will be shown hereunder, the expression for plane strain conditions will be preferred in some specific conditions.

The results (CPR versus K) are obtained because CGR-1 uses the expression for plane stress crack tip strain rate for the calculation of the 'constant function' G in expression (30). The equations (for plane stress and plane strain) are repeated hereunder and the expression of their ratio is shown in expression (79).

$$\dot{\varepsilon}_{ct(plane\ stress)} = \beta\left(\frac{\sigma_y}{E}\right)\left(\frac{n}{n-1}\right)\left\{\ln\left[\left(\frac{\lambda}{r}\right)\left(\frac{K}{\sigma_y}\right)^2\right]+\frac{1}{2}\ln\left[\left(\frac{\lambda}{r}\right)\left(\frac{K}{\sigma_y}\right)^2\right]^2\right\}^{\frac{1}{n-1}}\left(1+\ln\left[\left(\frac{\lambda}{r}\right)\left(\frac{K}{\sigma_y}\right)^2\right]\right)\frac{\dot{a}}{r} \tag{24}$$

$$\dot{\varepsilon}_{ct(plane\ strain)} = \beta\left(\frac{\sigma_y}{E}\right)\left(\frac{n}{n-1}\right)\left\{\ln\left[\left(\frac{\lambda}{r}\right)\left(\frac{K}{\sigma_y}\right)^2\right]\right\}^{\frac{1}{n-1}}\frac{\dot{a}}{r} \tag{16}$$

$$\frac{\dot{\varepsilon}_{ct(plane\ stress)}}{\dot{\varepsilon}_{ct(plane\ strain)}} = \frac{\left\{\ln\left[\left(\frac{\lambda}{r}\right)\left(\frac{K}{\sigma_y}\right)^2\right]+\frac{1}{2}\ln\left[\left(\frac{\lambda}{r}\right)\left(\frac{K}{\sigma_y}\right)^2\right]^2\right\}^{\frac{1}{n-1}}\left(1+\ln\left[\left(\frac{\lambda}{r}\right)\left(\frac{K}{\sigma_y}\right)^2\right]\right)}{\left\{\ln\left[\left(\frac{\lambda}{r}\right)\left(\frac{K}{\sigma_y}\right)^2\right]\right\}^{\frac{1}{n-1}}} \tag{79}$$

Expression (79) clearly shows that, for constant stress intensity, this ratio increases with lower yield strengths. This means that the function G in equation (30) becomes unreasonably high for lower yield strengths and explains the behaviour in Figure 7-1 and Figure 7-2. Expression (79) is visualized in Figure 7-3.

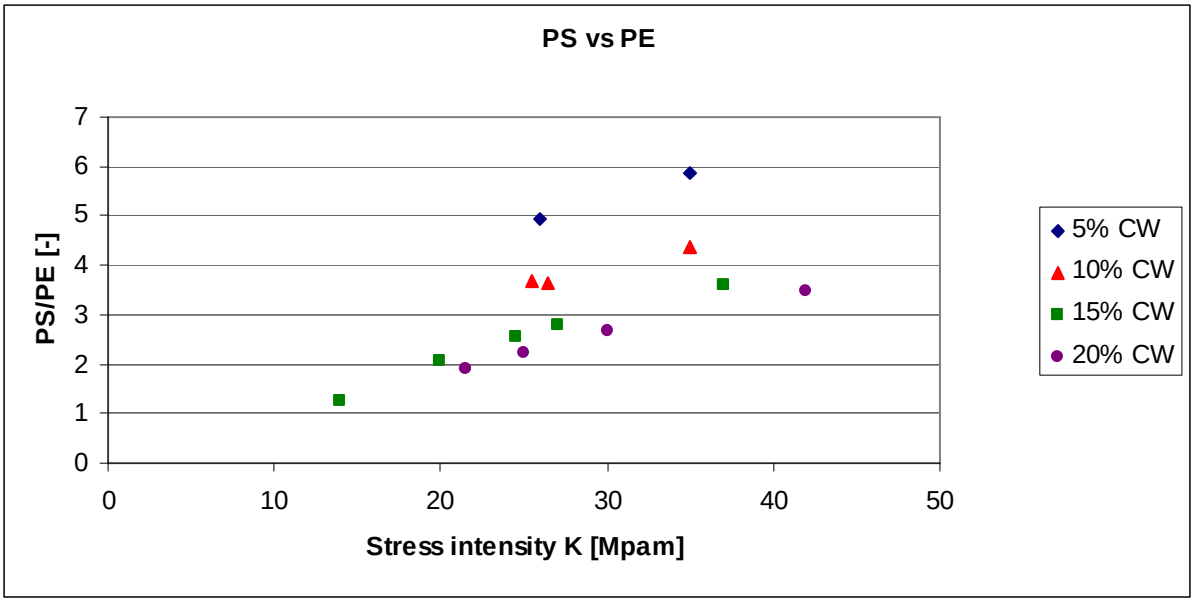

Figure 7-3: Plane stress (PE) versus plane strain (PE)

7.4 Plane stress or plane strain

There exists a criterion [22] whether plane stress or plane strain conditions are satisfied for a given specimen. This criterion relates the thickness of the specimen with the conditions at the crack tip and is frequently used in fracture toughness testing:

$$B \geq 2.5\left(\frac{K}{\sigma_y}\right)^2 \tag{80}$$

where B [mm] is the thickness of the specimen as indicated in Figure 5-3 and K and σ_y have their usual meaning and dimensions. If this criterion is satisfied, the plane strain formulation must be applied. In Table 7-1, expression (80) is applied on the cases that were discussed previously. Indeed, for some cases, plane stress (or strain) conditions are not valid and each case should be treated individually. The cases in italics in Table 7-1 should therefore be calculated with the plane stress formulation, the others with the plane strain formulation.

0.5TCT	**K [MPa√m]**			
B: 12.5 mm	30	25	20	15
σ_y [MPa]	**mm**			
243	*38,1*	*26,5*	*16,9*	9,5
345	*18,9*	*13,1*	8,4	4,7
495	9,2	6,4	4,1	2,3
572	6,9	4,8	3,1	1,7

Table 7-1: Verification of criterion (80)

7.5 CGR-1 with plane strain

All calculations carried out before can now be repeated, but in this case with the expression for plane strain crack tip strain rate in (30). The only modification is that a different function G is inserted in this expression. Obviously, these computations can not be accomplished by CGR-1, because only the expression for plane stress crack tip strain rate is internally programmed. Expression (30) comes into play for the calculation of the average current density, but the Etip-Itip relation provided by the environment does not change. This means that the calibration procedure that was used before can be reused, with the sole difference that the 'constant function' G will not be the same anymore.

The same approaches as previously described are also used again: an individual calibration against every data point, the best fitting of the data and the expression with the theoretical molar volume.

It is not necessary and interesting to repeat and show al successive steps, so only the results are shown hereunder in a few graphs and tables. These results are obtained after the calibration at the reference temperature 320°C and at varying temperatures.

Parameter	**Best fitting of the calculated data**	**Theoretical molar volume V_m**
Ea [J/mol]	**57517**	**66570**
Vm [m³/mol]	**2,06E-06**	**7,11E-06**
$\hat{\imath}^0_0$ A/m²	**2,57E+12**	**1,01E+13**

Table 6-7: Parameters in equation (77) with expression for plane strain crack tip strain rate

Best fitting of the calculated data			Theoretical molar volume V_m		
Case	i0-factor	CGR_calc [m/s]	i0-factor	CGR_calc [m/s]	CPR_meas [m/s]
1	2,45	1,07E-11	1,97	3,68E-12	**6,00E-12**
2	2,45	1,40E-11	1,97	4,79E-12	**1,50E-11**
3	2,55	1,77E-11	2,28	1,07E-11	**3,20E-11**
4	2,55	1,82E-11	2,28	1,10E-11	**1,60E-11**
5	2,55	2,25E-11	2,28	1,40E-11	**3,60E-11**
6	2,72	1,55E-11	2,83	1,88E-11	**4,50E-12**
7	2,72	4,79E-11	2,83	5,71E-11	**4,40E-11**
8	2,72	6,33E-11	2,83	7,44E-11	**4,40E-11**
9	2,72	6,85E-11	2,83	8,17E-11	**6,50E-11**
10	2,72	8,54E-11	2,83	9,87E-11	**1,10E-10**
11	2,81	7,73E-11	3,16	1,23E-10	**6,40E-11**
12	2,81	9,35E-11	3,16	1,44E-10	**1,10E-10**
13	2,81	1,07E-10	3,16	1,63E-10	**1,10E-10**
14	2,81	1,21E-10	3,16	1,73E-10	**1,80E-10**
15	0,98	1,07E-11	0,99	1,10E-11	**1,50E-11**
16	1,53	3,50E-11	1,62	4,60E-11	**2,80E-11**
17	2,81	1,07E-10	3,16	1,63E-10	**1,20E-10**

Table 7-2: Calibration against [22], results for plane strain expression

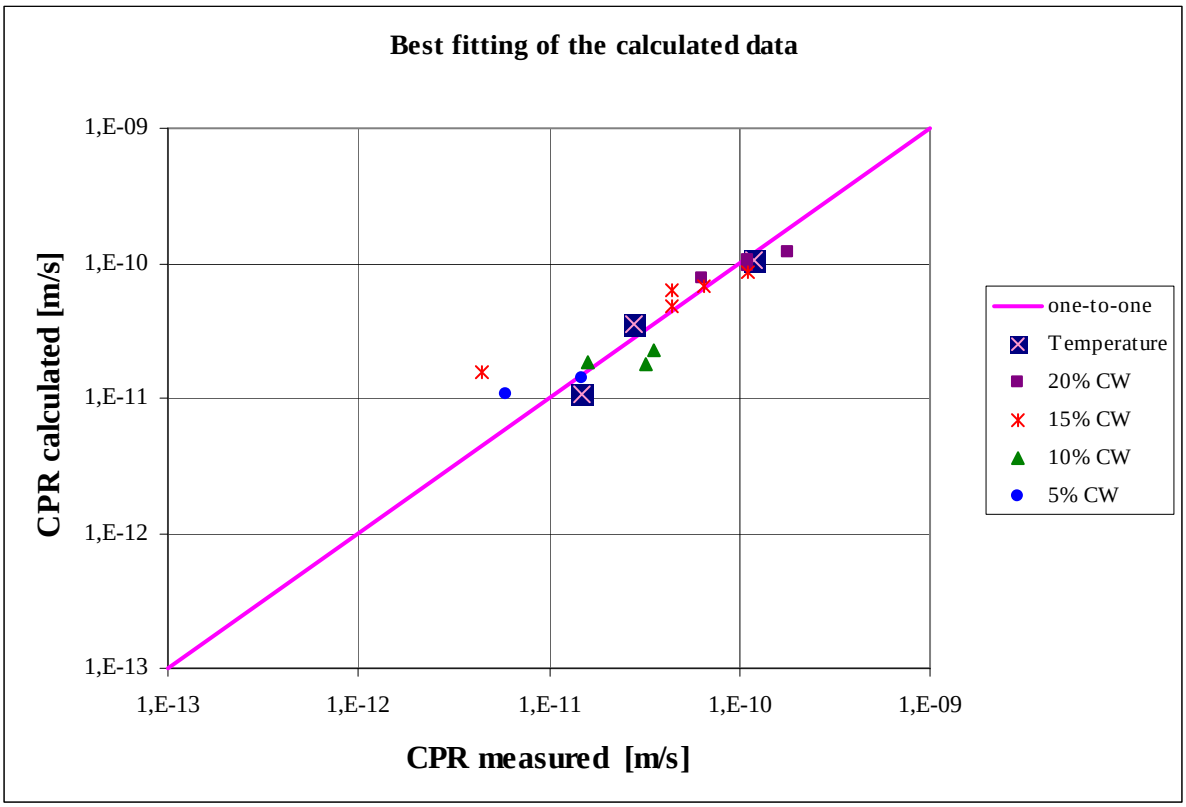

Figure 7-4: One-to-one plot of the measured and calculated crack propagation rates with best fitting of the calculated data plane strain conditions

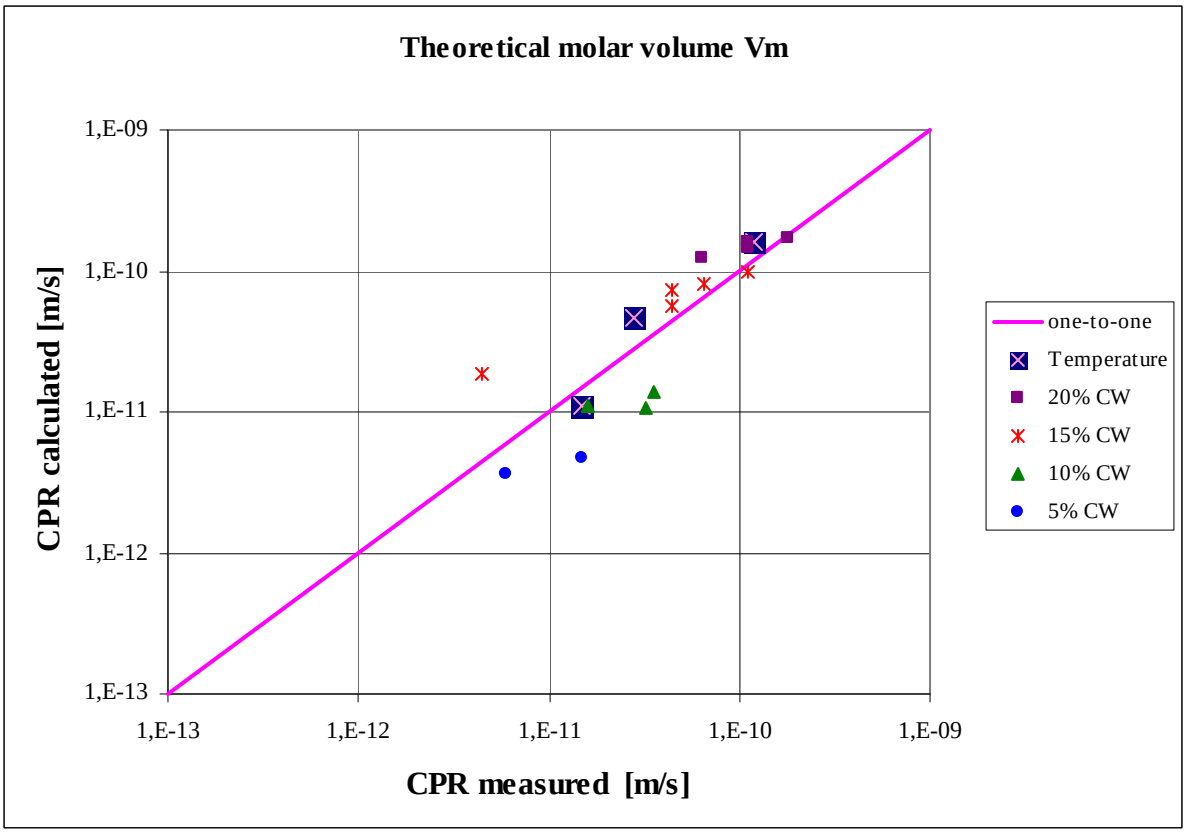

Figure 7-5: One-to-one plot of the measured and calculated crack propagation rates with the theoretical molar volume Vm data plane strain conditions

7.6 Discussion and conclusions

In general, the results in Figure 7-4 Figure 7-5 are better than those obtained for plane stress conditions. The results are also very good for those cases where criterion (80) is theoretically not applicable. The next step is to plot the equivalent graphs of Figure 7-1 and Figure 7-2, and to see if the CGR-K plot is more realistic for plane strain conditions.

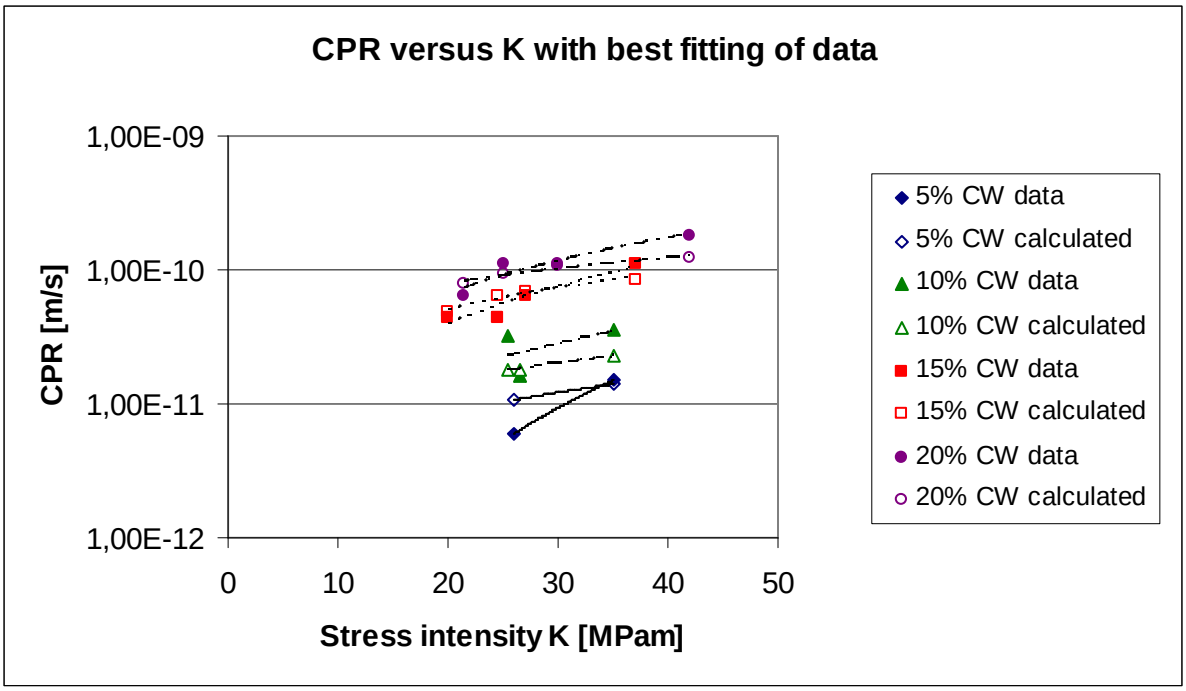

Figure 7-6: Stress intensity versus crack propagation rate with best fitting of the data under plane strain conditions

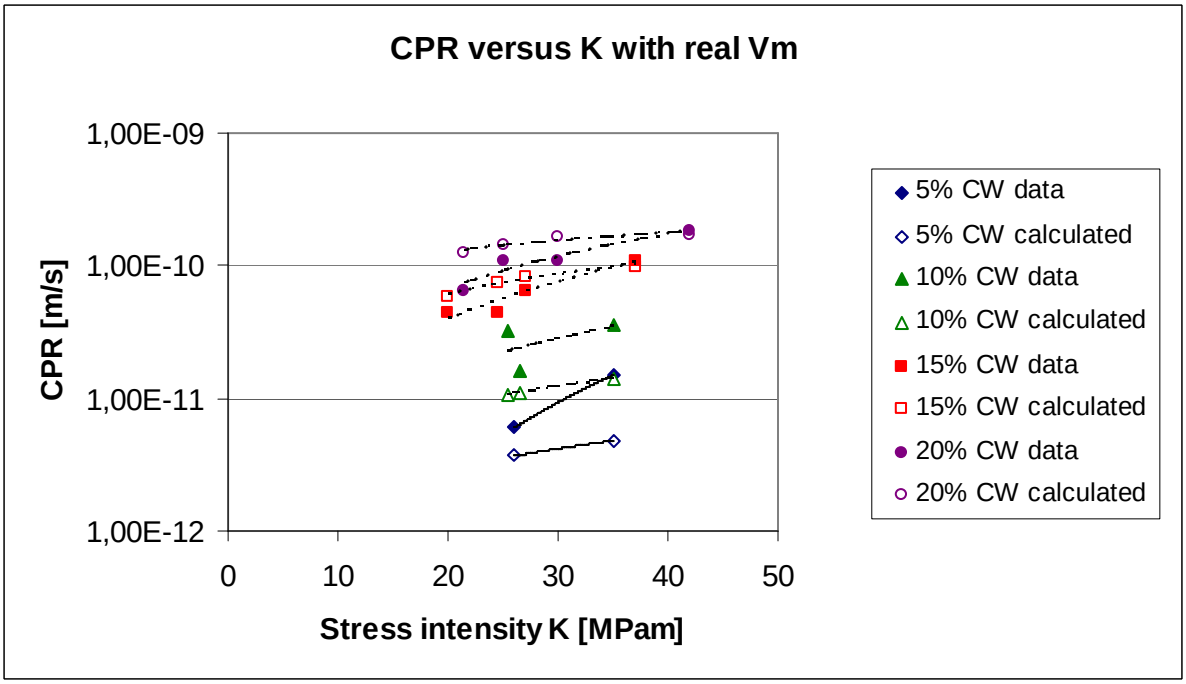

Figure 7-7: Stress intensity versus crack propagation rate with best fitting of the data under plane strain conditions

The new results are slightly better, compared to the ones in Figure 7-1 and Figure 7-2, but there is still some discrepancy at lower yield strengths.
As in section 6.4, the activation energy according to equation (78) can be acquired easily and the graphical result is shown in Figure 7-8.

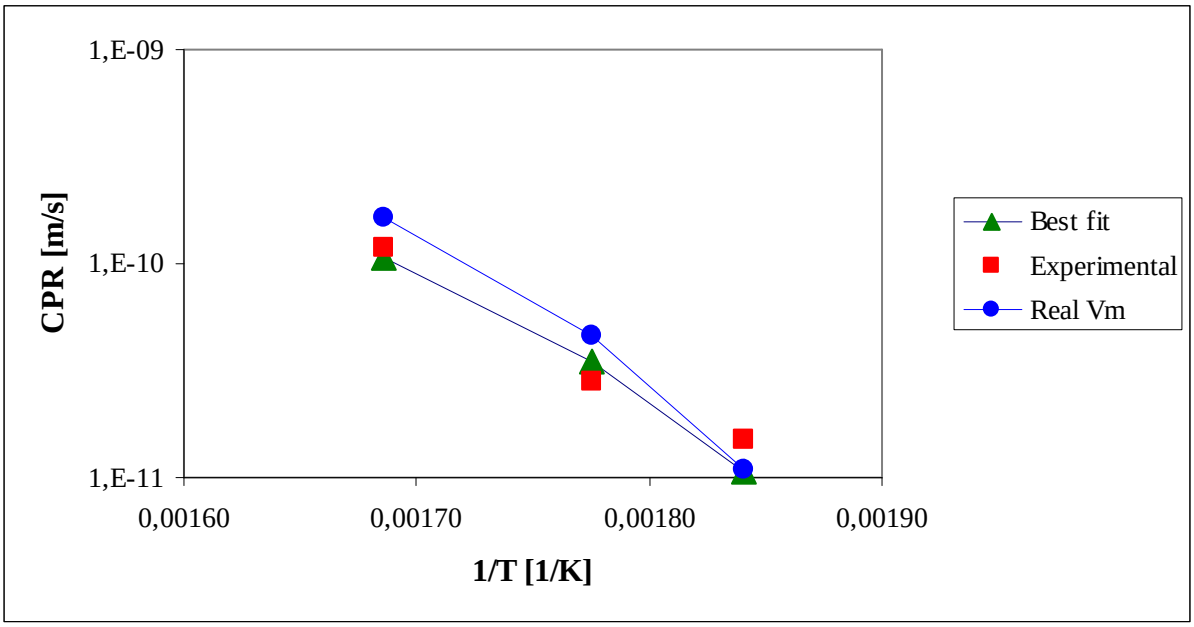

Figure 7-8: Temperature dependence of measured and calculated crack propagation rates under plane strain conditions

The activation energy for the best fitting is found to be 122.2kJ/mol, which is a good approximation of the experimental value (112.8kJ/mol). The acquired activation energy for the expression with the theoretical molar volume is 142.8kJ/mol, which is too much.

The remarks that were made so far, like the discussion plane stress/strain, will be bundled in the recommendations at the end of this thesis. This way, an overall overview of the suggestions for improvements is condensed in one specific section.
But, to finalize this discussion, it is obvious that the user should have the freedom to choose between both expressions in the user program and that both expressions should be implemented in the software.

8 Trend calculations with CGR-1

8.1 Introduction

Everything discussed so far has only been preparative work. The software is now fully calibrated and is ready to be used. The actual purpose CGR-1 is made for is to perform trend calculations to calculate crack propagation rates in a variety of situations.
First, the sensitivity to some parameters will be investigated: the influence of the repassivation parameter m and the crack length L. Up till now, these were kept constant as they were not well known anyway.
Then, the influence of fluid flow conditions will be studied by altering the Reynolds number, but one is limited to laminar flow. Finally, the influence of the concentration of dissolved species will be examined by altering the concentration of hydrogen, lithium and boron.
These trends will be calculated with the expressions for both plane stress and plane strain, so some comparison is possible. All trends are calculated with the more theoretical approach of the real molar volume as explained in the calibration procedures.
One arbitrary case (case 13) from the calibration is picked out and all trends will be calculated with respect to this reference case. Each time, only one input parameter will be changed.

8.2 Repassivation parameter m

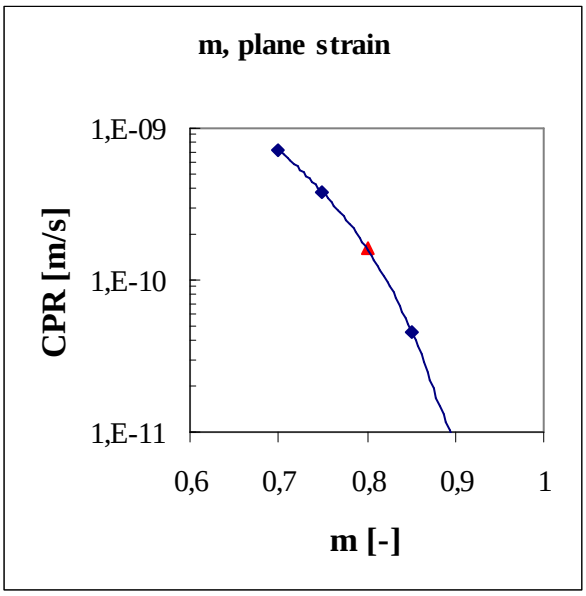

Figure 8-1: CPR-m under plane strain conditions

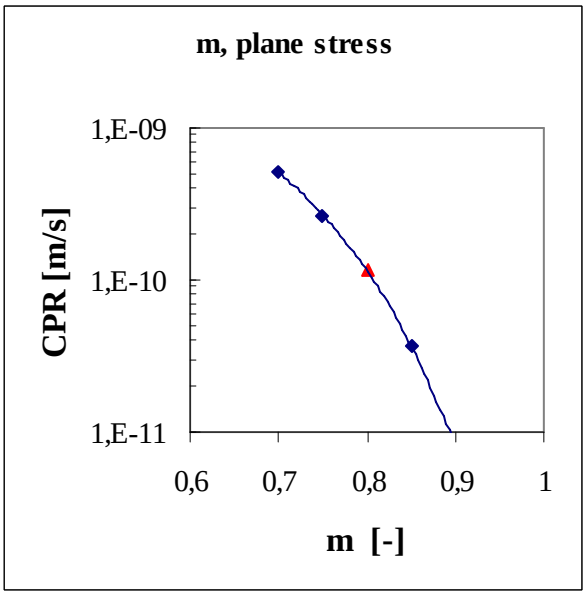

Figure 8-2: CPR-m under plane stress conditions

Figure 8-1 and Figure 8-2 clearly show the huge dependence of the crack propagation rate on the repassivation parameter. The observed trend is logical because an increase in m means that the passivating oxide layer recovers faster with less loss of material as a consequence. This is only valid if the film rupture time is the same in every situation.
This significant dependence can be derived from equation (30), where m appears between the square brackets and in the exponent. Even minute (~5%) deviations in m from the reference case lead to an increase or decrease of the crack growth rate of more than 100%.

8.3 Crack length L

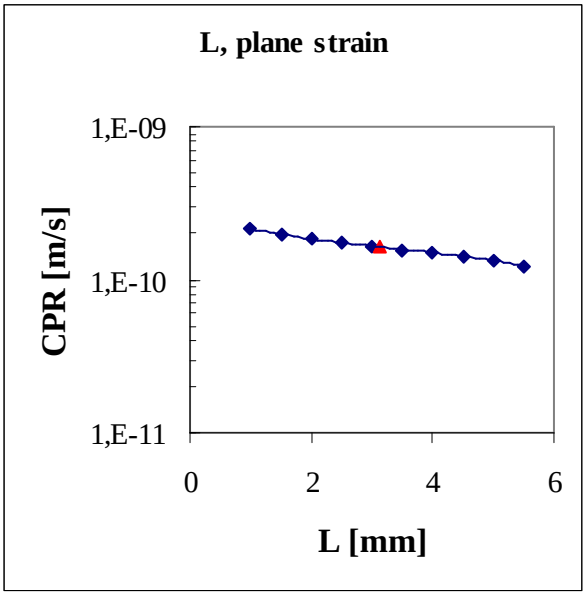

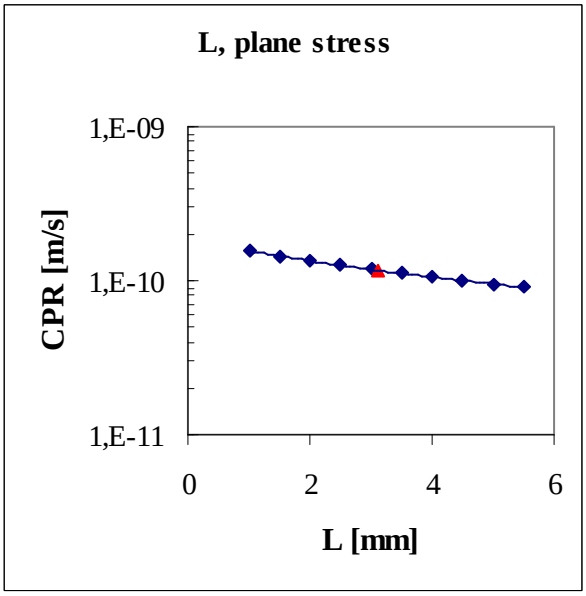

Figure 8-3: CPR-L under plane strain conditions **Figure 8-4: CPR-L under plane stress conditions**

The crack propagation rate is not very sensitive to the crack length, so the assumption made[15] before was not critical. Apparently, a crack length of 3.125mm is a good compromise value. A possible explanation is that the crack tip potential E_{tip} slowly decreases with increasing crack length. This decrease in potential is a favourable situation with respect to corrosion phenomena.

8.4 Reynolds number Re

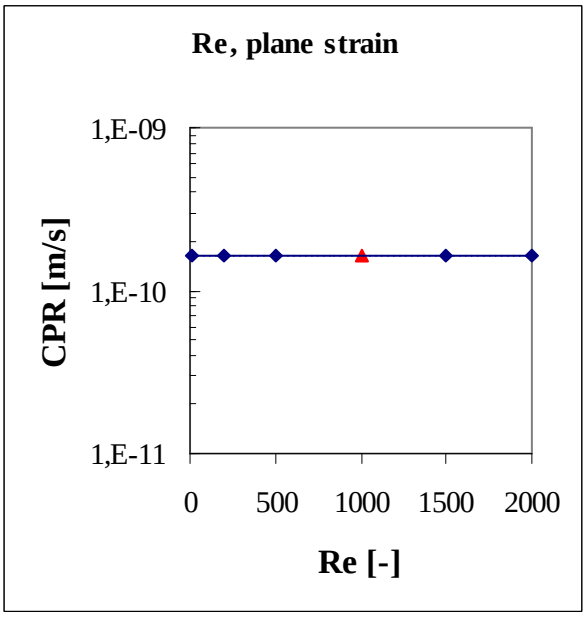

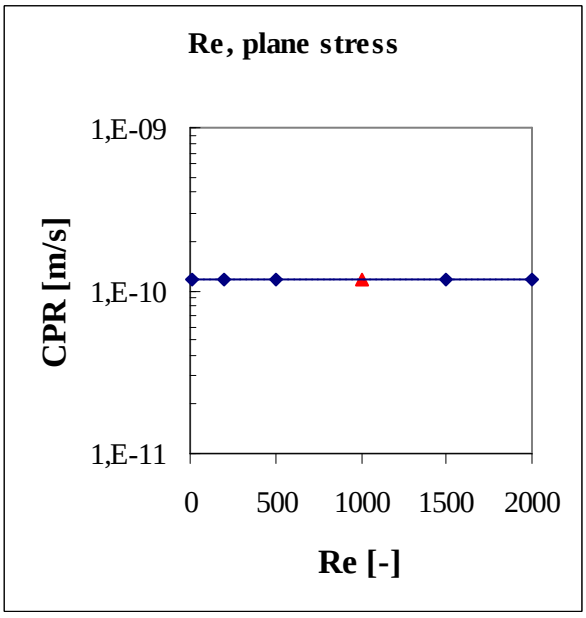

Figure 8-5: CPR-Re under plane strain conditions **Figure 8-6: CPR-Re under plane stress conditions**

The flow conditions, determined by the Reynolds number, seem to have no influence at all on the crack propagation rate. This looks rather awkward, because one could expect that

[15] See section 5.3

increasing fluid velocity (increasing Re) would increase the crack propagation rate, but apparently it does not. Increasing fluid flow replenishes the corrosive species at a much faster rate, but the conditions inside the crack remain more or less the same. Moreover, corrosion is assumed only to take place at the crack tip where the conditions (E, pH) do not change at all.

8.5 Hydrogen concentration H_2

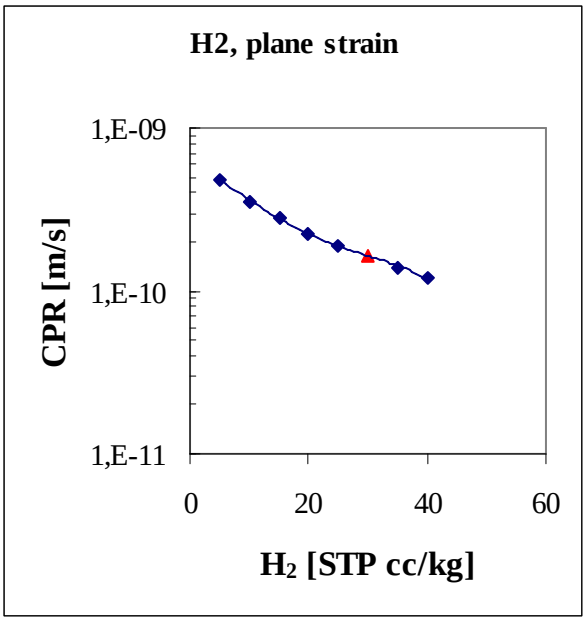

Figure 8-7: CPR-H2 under plane strain conditions

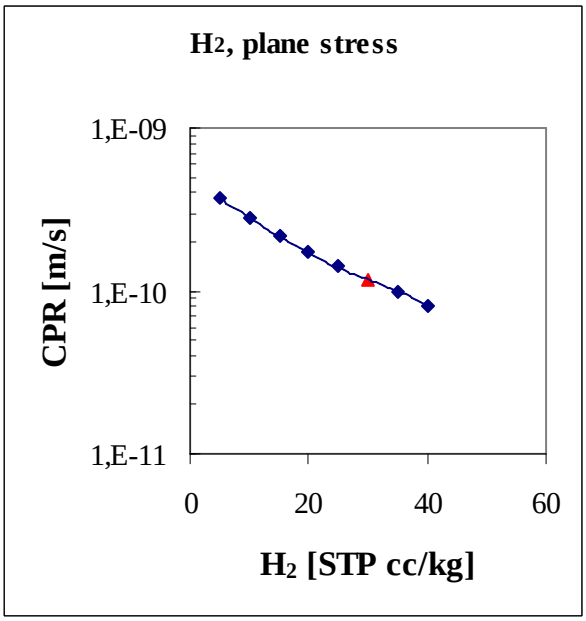

Figure 8-8: CPR-H2 under plane stress conditions

Hydrogen is added to the primary loop to minimize or avoid the presence of molecular oxygen that might leak in. The second purpose is to lower the electrode potential which, as already mentioned, is favourable with respect to corrosion phenomena. The graphs clearly show that increasing hydrogen content is significantly decreasing the crack propagation rate.

8.6 Boron and lithium concentration B, Li

Boric acid is added to the primary circuit to compensate for reactivity. In the beginning of a new cycle (BOC), the boron concentration is usually about 1000-1500ppm. This high acidic concentration dramatically lowers the pH in the loop, which enhances corrosion rates of the materials present. To compensate this, lithium hydroxide is added to maintain the pH in a range where corrosion rates are minimized. In practice, two different B-Li cycles are applied during the regular cycle in a PWR and these are represented [23] in Figure 8-9.

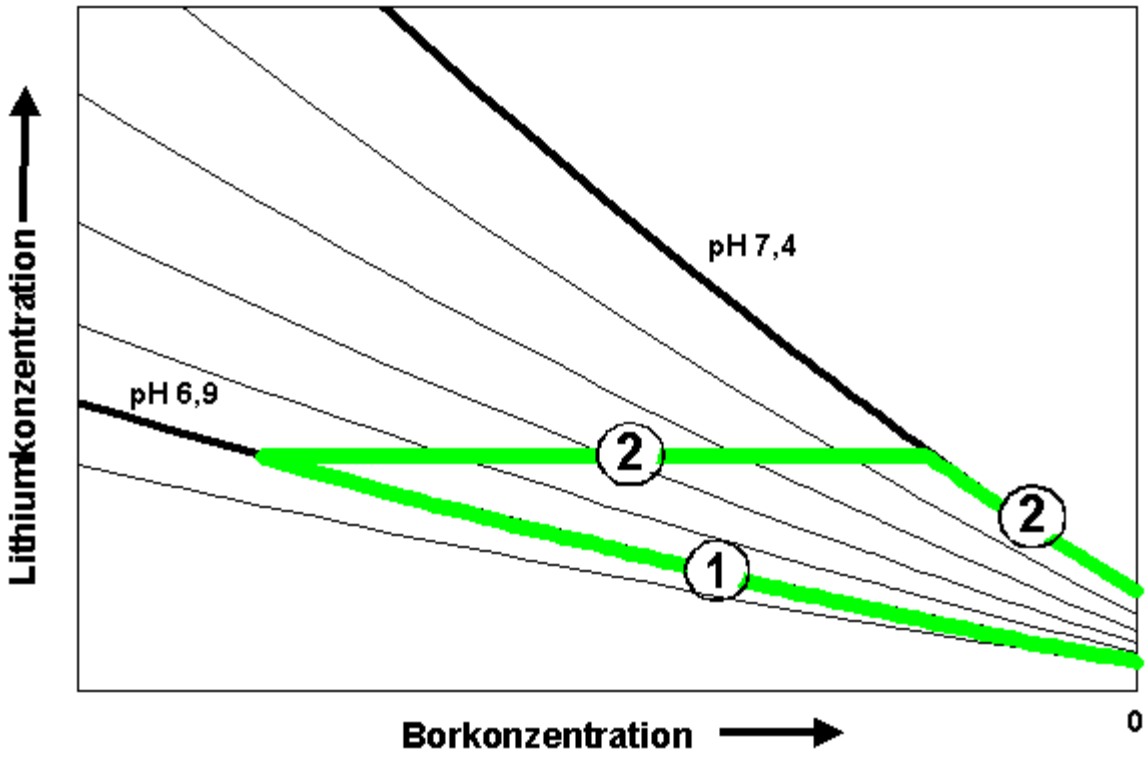

Figure 8-9: B-Li cycles in a PWR

The first cycle stabilizes the pH at a constant value of 6.9. This is accomplished by reducing the lithium hydroxide content, every time the operator of the reactor reduces the boron concentration as the cycle proceeds. The second cycle will keep the lithium concentration at 2ppm while the boron concentration reduces until the pH is 7.4. Then, for the rest of the duration of the cycle, the pH in the primary loop will be held at a constant value of 7.4. It should be noticed, however, that this is the pH in the bulk. Inside the crack, like in a crevice, the pH will differ a lot from that in the bulk fluid.

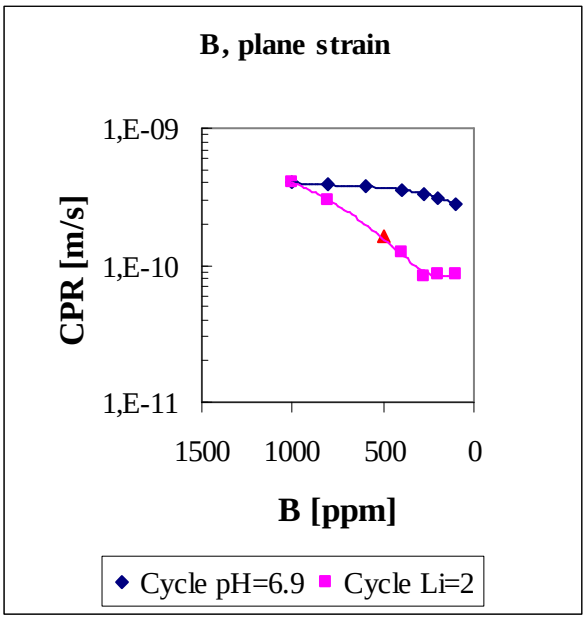

Figure 8-10: CPR-B under plane strain conditions

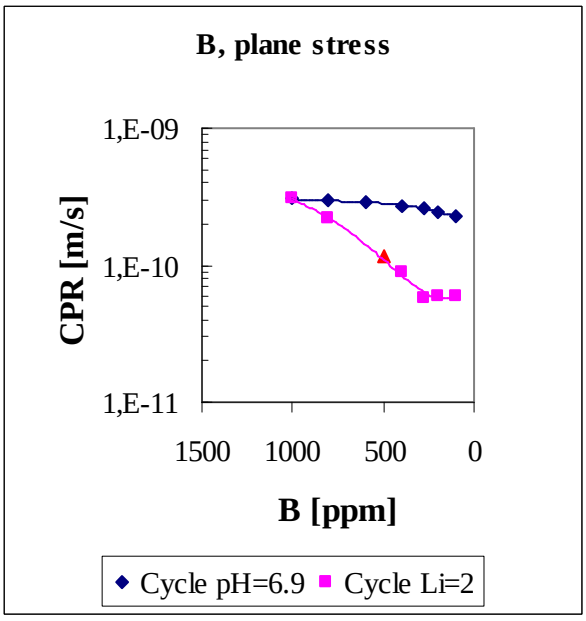

Figure 8-11: CPR-B under plane stress conditions

The two cycle types have an obvious influence on the crack propagation rate.
For the cycle with constant pH, the crack propagation rate remains rather constant as expected. Only at the end of cycle (EOC) the CPR reduces a little bit. This is probably due to the fact that the concentration of charged species is strongly reduced. This leads to a strong reduction of the conductivity and consequently the CPR.
For the second cycle, a significant decrease in crack propagation rates is observed[16]. The pH in cracks is usually lower than in the bulk. If the pH in the bulk increases towards 7.4, the pH in the crack will also rise slightly and will be higher at the crack tip than for cycle 1. The crack propagation rate at this higher pH is strongly reduced due to the preferential local conditions.

8.7 Conclusions

There is a wide variety of trend calculations that can be carried out with simultaneous variations of different input parameters. It is nevertheless instructive to investigate how one single parameter influences the crack propagation rate. The examples of trends computed in this section are all more or less logic. The main problem with this type of exercises is verification or validation of these obtained crack propagation rates with experimental data. According to [20], for instance, the observed growth rates does not change significantly with varying boron, hydrogen and lithium concentrations in normal PWR ranges. In the calculations, however, there is a difference between the maximum and the minimum CPR of about 400-500%. The question is therefore when one can talk about significant changes in crack growth rates as there is not a well defined limit or boundary.
Another interesting observation is that the predicted crack propagation rates for plane strain conditions are always higher than for plane stress, although the difference is not so very big. Moreover, the trends are similar for plane strain and plane stress.
As already mentioned in the discussion about input matrix during the calibration procedure, there is a huge uncertainty on the repassivation parameter, which is demonstrated here again.

[16] This significant decrease is in contradiction with other calculations (cfr. ECHEM) and might be a bug in the software code.

9 Recommendations and conclusions

9.1 Introduction

As final section of this thesis, some recommendations for improvements of the software code and the user interface will be summarized. Furthermore, some conclusions and final remarks concerning this thesis subject will be given.

9.2 Recommendations

The first remark is about the number of digits the user is allowed to insert in the user interface. The input parameters in Table 4-2 can be used to form an input matrix for the calculation of any specific case within the allowable range. The outcome is, for some parameters, very sensitive for the value that is inserted. Referring to the discussion on the sensitivity of the repassivation parameter, it is not possible at this moment to insert more than one digit after the comma. Although the code itself computes internally with more than one digit that is inserted, it is not displayed on the screen. The problem here is that, for instance, a value for m of 0.75 is displayed as 0.8 but the software does the calculations with 0.75. The consequence is that the correct value for the crack propagation rate is calculated, but the input matrix is displayed incorrectly which can lead to wrong conclusions. The difference in crack growth rate between an m value of 0.75 and 0.8 is indeed more than 500%. The same situation has been observed for input of the lithium concentration. The suggestion is therefore to allow the insertion of at least 2 additional digits after the comma for the parameters that have a large influence on the result.

A second remark concerns the reduction of the calculation time. The average time necessary to obtain a result is about 100 minutes, depending on the number of iterations. The suggestion is therefore to foresee a table where the user can insert an initial guess of the expected crack growth rate. An example of this can be seen in

Table 9-1.

Guess CPR [m/s]
default
10^{-9}
10^{-10}
10^{-11}
10^{-12}
10^{-13}

Table 9-1: Initial guess of crack propagation rate

This simple adjustement will avoid useless or unnecessary iterations if the user already knows in what range the calculated crack propagation rate will be. If this range is not yet known, a default CPR can be chosen and the iteration starts with an initial i_{avg} of 2A/m² as it was before.
A related subject is the highest value for i_{avg} that is executed. At this moment, it is set to 20A/m², which corresponds with a crack propagation rate of about 7.36 10^{-10}m/s. This means that, higher crack propagation rates can not be calculated.

The restriction to 20A/m² puts a serious burden on the applicability of CGR-1. Some realistic experimental crack propagation rates, for instance from [20], go up to 1 10^{-9}m/s and can therefore never be calculated. The recommendation concerning this observation is simply to raise the value for i_{avg} to 30 or even 40A/m². At least up to that value that corresponds with the highest experimental crack propagation rates. Nevertheless, a limitation is necessary to avoid the calculation of unrealistic crack growth rates that can lead to the making of erratic conclusions. These last two suggestions should reduce the calculation time and broaden the applicability.

Apart from the crack propagation rate, the user interface should also display the finally obtained value for the corrosion potential E_{corr}, the crack tip potential E_{tip} and the crack tip strain rate $\dot{\varepsilon}_{ct}$. This way, more useful information is provided on the screen and additional conclusions can be made more easily. Moreover, when the electrode potential is the subject of research, this can immediately be obtained from the output screen.

Two features in CGR-1, Export Tecplot and Save 3 Probe points, can be quite confusing. These tools can be used to store the data from the calculations in another format, WordPad for instance, which can be opened and stored on any computer. The problem with these tools is that the dimension of the concentration of the species is sometimes displayed as mol/l and sometimes as mol/m³. This depends on how the dimensions are set at the moment the tool is used, but the default settings are not necessarily the same. The suggestion therefore is to homogenize dimensions by making the default settings all mol/m³. If the user would then rather have his results in mol/l, the settings can be adapted manually.

More fundamental is the introduction in the code of the final formula (eq. 77) obtained after the calibration at variable temperatures:

$$\hat{i}_0 = \hat{i}_0^0 \exp\left(\frac{-E_a + \sigma_y V_m}{RT}\right) \tag{77}$$

The numerical values of the two variable parameters E_a (60467 J/mol) and $\hat{i}^0_0$ (1.23 10^{12} A/m²), as found in Table 6-3, can be added to the list of parameters. V_m, the theoretical molar volume, can be calculated from the molar mass M and the density ρ. These values are initial values and can be changed by the user if necessary, for instance after calibration with completely new experimental data. The code should be able to obtain a specific value for $\hat{i}_0$, for a given input matrix according to the given temperature and yield strength.
One should not forget that these values were obtained with an optimization method for only one set of experimental data. It is somewhat opportunistic to assume that these are completely correct. More experimental data is absolutely required to support the suggestions made here.

From the discussion in chapter 7, it is obvious that both expressions for plane stress/strain should be implemented in the software. Depending on the specimens used in the experiment and criterion (80), the user can decide whether plane stress of plane strain is applicable. Both equations should at least be available in the user interface, which is now only the case for plane stress.

All recommendations in this section make CGR-1 more user friendly, broaden the applicability and make it easier to draw the correct conclusions. These suggestions are quite easy to implement in the code or can be added to the user interface.

Further recommendations that can be made are mainly meant to assess more realistic PWR conditions. These suggestions are different from the ones already made, in the sense that these require a huge effort and a large amount of time to develop.
At this moment, no effects with respect to radiolysis are included. Radiolysis reactions will undoubtedly influence the crack propagation rates. Introducing these effects would imply a more realistic assessment with respect to IASCC.
Concerning fluid properties, the introduction of boiling phenomena and turbulent flow conditions would also improve the relevance of CGR-1.
These final recommendations can be seen as propositions for future developments if there is still interest in the assessment of crack growth rates.

9.3 Conclusions

This thesis has provided an extensive explanation of the slip dissolution model, the application of this model in the CGR-1 software .A calibration method has been discussed. Finally, some trend calculations regarding parameter sensitivity and realistic deviations from a reference case have been carried out.
The major shortcoming is definitely the unavailability of experimental data. Most calculations discussed in this thesis were referred only to one scientific article. Additional literature data concerning the experimental measuring of crack propagation rates was available [20, 24] but the applicability of these data was significantly limited. Information on the work hardening exponent, for instance, was not provided.
As CGR-1 is still in an experimental stage, a lot more dedicated experimental results are required to validate the calculations done by CGR-1. Furthermore, these experiments should provide all information necessary to assess all input data for CGR-1.
The results calculated by CGR-1 do not pretend to be completely predictive. Deviations with respect to experimental data of 100% or more are not unusual, but these inconsistencies are inevitable in the investigation of stress corrosion cracking. This is the case for experimental, as well as calculated crack propagation rates. This is supported by the observation that there is no international agreement on the underlying physical mechanism that is responsible for SCC. The mechanisms discussed in section 2.6 all have their merits and shortcomings, but the slip dissolution model is the only mechanism that has been developed mathematically. There have also been recent articles that seriously reject the slip dissolution/ film rupture model as it exists now. [25], for instance, indicates that this model is not yet a theoretical valid description. Moreover, [25] mentions that data presentations in log-log coordinates can diminish visually the discrepancy in experimental and computed results and that the model can contain inconsistencies and contradictions. According to [26] on the other hand, the crack tip strain rate has much too weak dependency on the loading rate $\dot{K}$. In CGR-1, this loading rate is assumed zero to obtain a closed analytical formula for the calculation of the crack propagation rate. This article also mentions an extreme sensitivity of some parameters (r, n) in the expression for the crack tip strain rate on the CPR for variable values of m.
All these comments, positive or negative, illustrate the absolute necessity for further improvements of this model.
As CGR-1 is based on this analytical expression, inconsistencies between calculated and experimental data are unavoidable. The actual purpose of CGR-1 is to perform trend calculations with respect to stress corrosion cracking and this is feasible, but verification remains absolutely necessary.

10 References

1. BNEN course: Nuclear Materials II, part of W. Bogaerts, 2007.
2. R.H. Jones, R.E. Ricker, Mechanisms of Stress-Corrosion cracking, in: R. H. Jones (Ed.), Stress-Corrosion Cracking, Materials Performance and Evaluation, ASM International, ISBN 0871704412, 1992.
3. F.P. Ford, Slip dissolution model, in: D. Desjardins, R. Oltra (Eds.), Corrosion sous contrainte – Phénoménologie et méchanismes, Bombannes, 1990.
4. P.L. Andresen, F. P. Ford, Materials Science and Engineering, A103, 1988.
5. D. D. Macdonald, M. Urquidi-Macdonald, Corrosion Science 32, 1991.
6. T. Shoji, S. Suzuki, R. G. Ballinger, NACE Vol. 2, 1995.
7. T. Shoji, Z. Lu, Q. Peng, S. Wang, Y. Takeda, A. Kai, PVP2004-2662, 2004.
8. Y.C. Gao, K.C. Kwang, Proc. 5th International Conference on Fracture, France, Vol 2, 1981.
9. T. Shoji, K.S. Raja, G.F. Li, Y.J. Lee, A. Brozova, Corrosion/2000, NACE, Paper 00190, 2000.
10. A. Turnbull, Corrosion Science 39, 1997.
11. S. Gavrilov, M. Vankeerberghen, Numerical simulation of IASCC, Convention Electrabel SCK•CEN R3841, 2004.
12. J.S. Newman, Electrochemical Systems, 2nd edition, Prentice-Hall, 1991.
13. M. Vankeerberghen, S. Gavrilov, Radio-electrochemical calculations in respect of stress corrosion cracking, Convention Electrabel SCK•CEN R-4334, 2006.
14. K. Arioka, T. Yamada, T. Terachi, G. Chiba, Corrosion 63(12) 1114, 2007.
15. ASME code Part 2D - edition 1995.
16. Li H. Wang, C.H. Tsai, J.J. Kai, Repassivation kinetics of irradiated stainless steel in high temperature water, ICG-EAC Meeting April 22-27, 2001.
17. EPRI NP-5064M Project 2006-6 Final Report February 1987: Corrosion-Assisted Cracking of Stainless and Low-Alloy Steels in LWR Environments, 1987.
18. E.M. Gutman, Mechanochemistry of solid surfaces, World Scientific Publishing, ISBN 9810217811, 1994.
19. M. Vankeerberghen SCK•CEN Internal Report I-120, 2007.
20. EPRI-CIR Report 1007380.
21. K. Arioka, private communication.
22. ASTM E 399-90.
23. M. Jürgensen, H. Neder, D. Wolter, U. Staudt, S. Odar, V. Schneider, VGB guideline for the water in nuclear power plants with light water reactors (PWR) VGB-R 401 J, 2006.
24. T.M. Karlsen, M. Espeland, Á. Horváth, Summary report on the PWR crack growth rate investigation, IFA-657, OECD Halden Reactor Project, HWR-773, 2005
25. E.M. Gutman, Corrosion Science 49, 2007
26. R.C. Newman, C. Healey Corrosion Science 49, 2007

11 List of figures

Figure 2-1: Interactions between material, radiation, environment and stresses 2
Figure 3-1: Representation of the crack as interface between the environment and the material 8
Figure 3-2: Current density profile at the crack tip 9
Figure 4-1: 2D representation of crack geometry Figure 4-2: 3D representation of crack geometry 17
Figure 4-3: Flow chart of the calculation procedure of CGR- 23
Figure 5-1: Schematic representation of the calibration procedure 24
Figure 5-2: Temperature dependency of Young's elasticity modulus 26
Figure 5-3: Schematic representation of a 0.5CT specimen 26
Figure 5-5: Fitting of calculated data and theoretical approach Vm 29
Figure 5-6: One-to-one plot of calculated and measured crack propagation rate after
Figure 5-7: One-to-one plot of calculated and measured crack propagation rate after calibration with theoretical molar volume Vm 31
Figure 6-1: Temperature dependence of yield strength 35
Figure 6-2: Graphical results for the calibration at varying temperatures and at 320°C 36
Figure 6-3: One-to-one plot of the measured and calculated crack propagation rates with best fitting of the calculated data 37
Figure 6-4: One-to-one plot of the measured and calculated crack propagation rates with the theoretical molar volume 38
Figure 6-5: Temperature dependence of measured and calculated crack propagation rates 39
Figure 7-1: Stress intensity versus crack propagation rate with theoretical molar volume 40
Figure 7-2: Stress intensity versus crack propagation rate with best fitting of the data 41
Figure 7-3: Plane stress (PE) versus plane strain (PE) 42
Figure 7-4: One-to-one plot of the measured and calculated crack propagation rates with best fitting of the calculated data plane strain conditions 44
Figure 7-5: One-to-one plot of the measured and calculated crack propagation rates with the theoretical molar volume Vm data plane strain conditions 45
Figure 7-6: Stress intensity versus crack propagation rate with best fitting of the data under plane strain conditions 46
Figure 7-7: Stress intensity versus crack propagation rate with best fitting of the data under plane strain conditions 46
Figure 7-8: Temperature dependence of measured and calculated crack propagation rates under plane strain conditions 47
Figure 8-1: CPR-m under plane strain conditions Figure 8-2: CPR-m under plane stress conditions 48
Figure 8-3: CPR-L under plane strain conditions Figure 8-4: CPR-L under plane stress conditions 49
Figure 8-5: CPR-Re under plane strain conditions Figure 8-6: CPR-Re under plane stress conditions 49
Figure 8-7: CPR-H2 under plane strain conditions Figure 8-8: CPR-H2 under plane stress conditions 50
Figure 8-9: CPR-B under plane strain conditions Figure 8-10: CPR-B under plane stress conditions 51
Figure 8-11: B-Li cycles in a PWR 51